POLITECNICO DI TORINO

Corso di Laurea in Ingegneria Meccanica

Tesi di Laurea Magistrale

Equilibrium Droplet Shapes on Micro-Textured Biomimetic Surface

Relatore
prof. Pietro Asinari

Laureando
Luca BELLORA
matricola: 242394

ANNO ACCADEMICO 2017 − 2018

ACKNOWLEDGMENTS

TABLE OF CONTENTS

LIST OF TABLES

LIST OF FIGURES

LIST OF ABBREVIATIONS

2PP	Two-Photon Polymerization
AM	Additive Manufacturing
CAD	Computer-Aided Design
CSV	Comma Separated Value
DXF	Drawing Exchange Format
FBMS	Fixed-Beam-Moving-Sample
GUI	Graphical User Interface
IGES	Initial Graphics Exchange Specification
ITO	Indium Tin Oxide
LSE	L Surface Evolver
MBFS	Moving-Beam-Fixed-Sample
MNFTL	Micro-/Nanoscale Fluid Transport Laboratory
NCF	Nanotechnology Core Facility
ODE	Ordinary Differential Equation
PSF	Parameter Sweep Function
PPGT	Professional Photonic GT
SE	Surface Evolver

LIST OF ABBREVIATIONS (continued)

SE-FIT   Surface Evolver - Fluid Interface Tool

SEM   Scanning Electron Microscope

STL   Standard Triangle Language

UIC   University of Illinois at Chicago

SUMMARY

In the arid desert region of Namibia (Africa), there exists a particular type of beetle known as *Onymacris unguicularis*. Living in a very arid region with very little rainfall, these insects rely on fog to quench their thirst. Previous research including a recent BBC production TV series named as *Planet Earth II* has shown this amazing behavior of the insects. Their behavior has inspired multiple studies over the years but the fundamental mechanics of fog interaction with their back shell (aka *elytron*) is yet to be completely understood. The current study is focused on analyzing this liquid-solid interaction using computational tools.

A computational analysis of water droplet spreading over a beetle inspired micro-textured model is conducted, supported by live observation of water interaction on a likewise designed 3D printing sample. The target of the research is understanding the effects of such morphology on water collection, in light of capillarity, wetting phenomena and biological significance.

This thesis investigates wetting interfaces, by means of numerical modeling through an open-source Visual BASIC .NET based program. Particularly, the analysis focuses on the air/water interfacial area, which is proved to reduce for droplets deposited on the micro-textured surface, with respect to identical droplets on smooth flat surfaces. Some hypotheses about the influence of such reduction on evaporation are formulated, considering their biological significance.

Further developments of the analysis are suggested, to achieve a more complete understanding of the phenomenon.

SUMMARY

Nell'arida regione desertica della Namibia, vive una particolare specie di scarabeo nota come *Onymacris unguicularis*. A causa delle ardue condizioni di vita del deserto africano, con precipitazioni scarse e rare, questi insetti si affidano a banchi di nebbia per soddisfare la loro sete. Diverse ricerche precedenti, tra cui una recente produzione televisiva della BBC, *Planet Earth II*, hanno mostrato il comportamento straordinario di questi insetti: essi quando hanno bisogno di bere, scalano le dune per esporre il loro guscio a dei venti nebbiosi, caratteristici del deserto namibiano, raccogliendo su di esso gocce d'acqua. Nonostante tali osservazioni abbiano ispirato negli anni numerosi studi, la meccanica alla base dell'interazione delle particelle d'acqua provenienti dalla nebbia con il loro guscio deve ancora essere globalmente compresa. Il presente studio si concentra sull'analisi di tale interazione liquido-solido, attraverso l'utilizzo di strumenti computazionali.

Viene quindi condotta un'analisi computazionale di gocce d'acqua di vari volumi che si depositano su un modello microstrutturato ispirato al guscio dello scarabeo. Tale risultato è ulteriormente supportato dalla diretta osservazione dell'interazione dell'acqua su un campione similmente progettato e stampato tridimensionalmente. L'obiettivo della ricerca è comprendere gli effetti di tale morfologia sulla raccolta dell'acqua, alla luce dei fenomeni di capillarità, bagnabilità e delle caratteristiche biologiche dello scarabeo.

Questa tesi analizza delle interfacce di bagnatura, per mezzo di modellazione numerica con un programma open-source basato su sintassi Visual BASIC .NET. In particolare, lo studio si

SUMMARY (continued)

focalizza sulla superficie interfacciale aria/acqua, che dimostra di ridursi per gocce depositate

sulla superficie microstrutturata, rispetto a ciò che accade per gocce identiche su una superficie

ideale piatta e liscia. Vengono quindi formulate alcune ipotesi sull'influenza di tale riduzione

sull'evaporazione, considerando il contesto biologico in cui vive lo scarabeo. Sono inoltre sug-

geriti ulteriori sviluppi di questa ricerca, al fine di ottenere una comprensione più completa del

fenomeno.

CHAPTER 1

INTRODUCTION

History of technology has frequently witnessed new inventions inspired by Nature. Engineering is rich with examples of techniques, components and devices deriving from Biomimetics: for instance, *Velcro* was invented in the 1940s inspired by burdock seeds clinging on clothes [3], the aerodynamics of *Shinkansen* Japanese high-speed train is based on the kingfisher bird's beak in order to minimize on-board noise [4], and from sharks' skin repellency to algae a special protective coating for reducing blades' erosion on wind turbines was developed by the *3M* company [5].

Similarly, in 1976 Hamilton [6] reported an interesting discovery that inspired many following studies: a species of beetles from Namibia (*Onymacris unguicularis*) could survive in desert environment by collecting water droplets on its shell (aka. *elytron*) for drinking purpose. As a matter of fact, Namib desert is characterized by winds transporting dense fog banks, representing its only water source. Particularly, evolution led these beetles to adapt to such inhospitable environment, developing fog-harvesting skills: the insects spend the majority of their life underneath the sand, whose temperature deep varies around $30 - 35°C$, much more habitable compared to the sun exposed surface at $75°C$. Here, they spend their time without eating, nor drinking for up to 70-80 days at a time. Then, to quench their thirst, they move out of sand, climb the high dunes of the desert and address their shell to the foggy wind, standing on their heads to maximize the wind flux, which deposits water droplets on the micro-patterned back.

Subsequently, other species of beetles were found to show analogous behavior, leading to several studies on these insects' elytron, which have triggered controversies on its interfacial properties: one of the pioneering published work is by Lawrence and Parker [7], who have reported that *Stenocara dentata* beetles present a characteristic roughness due to bumps distribution on their back. Furthermore, differences in wettability were noticed between the bump tips and the separating grooves, coated with a special wax making them hydrophobic. As a result, *Stenocara dentata* beetles show wettability patterned backs, with hydrophilic bump tips where water is collected and coalesces, and hydrophobic waxed valleys where the droplets roll down to the mouth: through such procedure, the beetles can "store" water for the weeks they spend underground. Similar bumpiness was discovered on *Onymacris unguicularis* beetle's shell, which pushed scientists to research whether wettability patterning is present on their elytron, too.

Engineering interest towards such micro-textured surface arises when coping with fog-collecting surfaces, such as water-trapping tents, building coverings and water collecting devices. For instance, *Yanko Design* was inspired by the desert beetle to design its *Dew Bank Bottle* [8], able to collect potable water from the morning dew: water condenses over its cool steel surface, rolling down to a narrow gap where droplets are collected to a storage tank. The Dew Bank Bottle's working principle is water condensation: an innovation would be achieved by beetle-like micro-patterning the metal surface of the water collecting device, to work by droplet deposition. Since this discovery, observations of water collection on dead beetles' shells have been executed. However, all the experiments were led on dead beetles so far, to our knowledge. Hence, the Micro-/Nanoscale Fluid Transport Laboratory (MNFTL) at the University of Illinois at Chicago
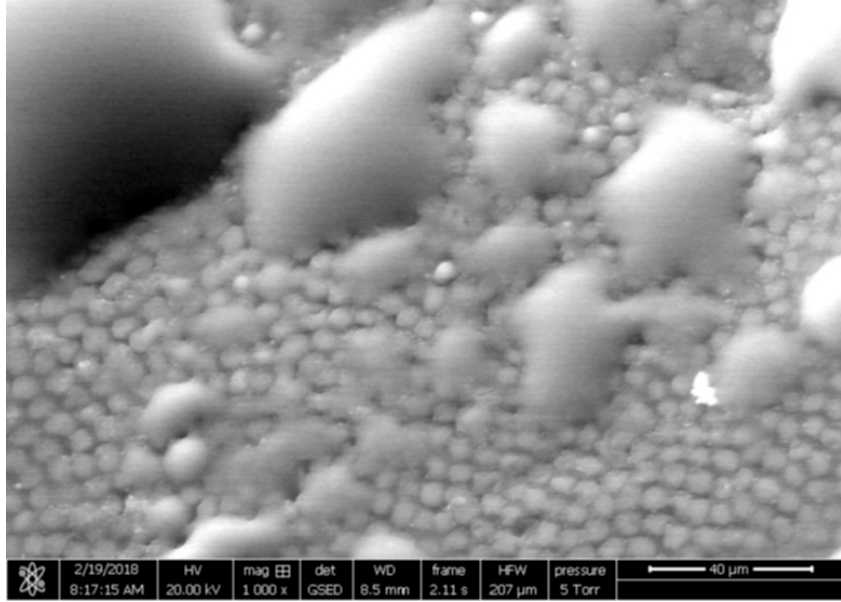
Figure 1: Water droplets deposited on *Onymacris unguicularis* beetle's shell.

(UIC) attempted to study live beetles, observing them while capturing water droplets from a simulated fog flow.

In addition, observations of elytron samples in high humidity environment were conducted, to inspect the shape of the formed water droplets. As shown in Figure 1, no characteristic droplet shape is observed: water deposits around the bumps without any special preferential direction. This led the research group to further investigate the interaction of small water droplets with the micro-textured surface.

In order to more deeply assess this observation, computational analysis is useful to better understand the droplet spreading on such a textured surface: as a matter of fact, the observed water droplets' magnitude is the *picoliter* (pL), namely $10^{-12}\,L = 10^{-15}\,m^3$, too small a scale

to develop a physical testing system. The software involved (*SE-FIT*, deeply described in chapter 3) starts from the physics of the problem to converge the system "droplet/wet wall" to an equilibrium condition, through potential energy minimization. In order to grasp the program's utility, the following chapter contain some background material on wettability and capillarity-related phenomena, providing the reader with the basic instruments to understand the physics of the treated problem.

CHAPTER 2

THEORETICAL BACKGROUND

Capillarity is the branch of Fluid Mechanics analyzing the behavior of liquid interacting with other immiscible fluid phases [9]. It can concentrate on liquid/liquid or liquid/gas interface study: particularly, in the latter case, most of the times the gas phase is constituted by air. It is crucial to understand the physical laws governing the deformation of such interfaces, which adapt their shape to seek the equilibrium, which is reached when the interface's surface energy is minimum.

2.1   Surface Tension

When a liquid interacts with an immiscible fluid (another liquid or a gas), an interface between the two phases is originated. For example, one can consider an oil drop immersed in water, or a soap bubble floating in air, assuming a characteristic spherical shape. The formation of such interface requires an energy cost from both the involved substances, which logically tend to the condition of minimum energy expense. Hence, since the spherical shape presents the least surface-area-to-volume ratio, it represents the most suitable geometry to assume for the immersed phase.

From this intuitive explanation, it is possible to define the surface energy per unit area spent by the two phases to form the separating interface, namely the *surface tension*, γ. Particularly,

the surface tension can be defined as the work δW required to enlarge the surface of a liquid by a unit area dA. Consequently, one has:

$$\delta W = \gamma \, dA \qquad (2.1)$$

Alternatively, surface tension can be defined through an analogy with Solid Mechanics. As a matter of fact, the dimension of γ is energy per unit area. By the following elaboration, it is possible to notice that:

$$[\gamma] = \frac{E}{L^2} = \frac{F \cdot L}{L^2} = \frac{F}{L} \qquad (2.2)$$

From a mechanical point of view, the separating surface between the liquid and the second phase behaves like an elastic membrane subject to a uniform stress field. For example, if one imagines to section a solid membrane along a segment of length L, the internal forces acting on the two patches to stick them together can be individuated. Similarly, if one cuts a liquid surface into two, an analogous force F is acting to keep the surface coherent. Surface tension can be defined as the capillary force per unit length acting on the liquid surface to keep it uniform. Hence, surface tension may be described in units of either J/m^2 or N/m. However, typical magnitude order of surface tension is $[mN/m] = [mJ/m^2]$: water presents pretty a high surface tension against air, approximately equal to $72 \, mJ/m^2$, due to hydrogen bonds between its molecules.
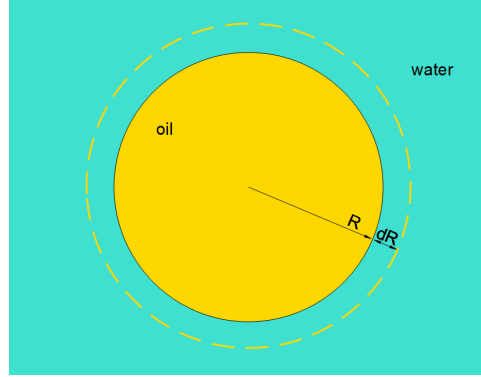
Figure 2: Scheme for derivation of Laplace pressure for a spherical drop of water in oil.

2.2   Laplace Pressure

In order to maintain the spherical shape, pressure inside drops and bubbles needs to be higher than outside. This overpressure, called *Laplace pressure*, originates as a consequence of the surface tension between the two interacting phases.

Considering a drop of oil in water, it assumes the shape of a sphere with radius R, as explained in 2.1. As shown in Figure 2, for an infinitesimal enlargement dV of the drop's volume, it is necessary to shift the oil/water interface by a displacement dR. Such new configuration is obtained through an infinitesimal work δW, executed by capillary force and by the pressure forces in both oil, p_{oil} and water, p_{water}, evaluable as follows:

$$\delta W = p_{oil}\, dV - p_{water}\, dV + \gamma_{oil/water}\, dA \tag{2.3}$$

where $dV = 4\pi R^2\, dR$ is the increment in volume of oil, equal to the reduction in volume of water, and $dA = d(4\pi R^2) = 4\pi \cdot 2RdR = 8\pi RdR$ is the variation of oil/water interface. By substituting these results into Equation 2.3 and imposing the mechanical equilibrium condition $\delta W = 0$, it is possible to obtain the following expression for Laplace pressure:

$$\Delta p = p_{oil} - p_{water} = \frac{2\,\gamma_{oil/water}}{R} \tag{2.4}$$

Generalizing the problem to any interface geometry, it is possible to demonstrate that the Laplace pressure is directly proportional to the curvature C of the interface, and the proportionality constant is the surface tension between the two phases. This is known as the *Laplace's theorem*, expressed by the following relation:

$$\Delta p = \gamma C = \gamma \left(\frac{1}{R_1} + \frac{1}{R_2} \right) \tag{2.5}$$

where subscripts 1 and 2 indicate the two perpendicular reference axes used to calculate the curvatures.

2.3 Wetting

In section 2.1, the described floating liquid drops maintained their spherical shape. However, when the liquid gets in touch with a solid substrate, *wetting* phenomenon develops, leading to different drop configurations, depending on the nature of the three involved phases (solid substrate, liquid and air).

Considering an ideal smooth substrate, it is possible to distinguish among two types of wetting,

according to the liquid's affinity for the solid [9]: in *total* wetting, the liquid spreads completely

on the solid substrate, whereas if wetting is *partial*, the liquid deposits assuming the shape of

spherical cap, intersecting the solid substrate with a *contact angle θ_E*.

Particularly, these two situations can be distinguished based on a *spreading parameter S*, namely

the difference between the dry and wet condition of the substrate in energy per unit area, given

by the involved surface tensions:

$$S = \gamma_{sa} - (\gamma_{sl} + \gamma_{la}) \tag{2.6}$$

where the subscripts indicate the two phases involved for each surface tension term (solid, liq-

uid, air). If surface energy in dry condition is higher $(S > 0)$, the liquid spreads over the

substrate, and there is no contact angle $(\theta_E = 0)$. Vice versa $(S < 0)$, wetting is defined as

partial $(\theta_E \neq 0)$.

Since the analyzed substrate presents partial wetting, the present study is interested in deep-

ening the latter case: the contact angle on a solid surface can be calculated imposing the me-

chanical equilibrium condition to the liquid drop. From the free body diagram of the contact

line, illustrated in Figure 3:

$$\gamma_{vs} = \gamma_{ls} - \gamma cos\theta_E \tag{2.7}$$
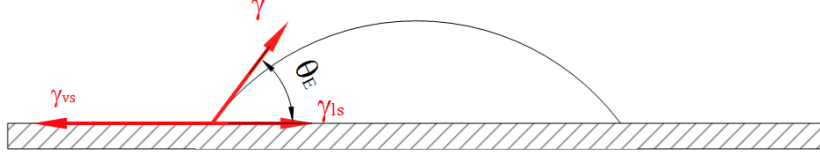
Figure 3: Determination of θ_E through projection of forces acting on the contact line.

Hence, it is possible to obtain *Young's relation* for the equilibrium (or *static*) contact angle, characterizing each pair of liquid and material:

$$\cos\theta_E = \frac{\gamma_{ls} - \gamma_{vs}}{\gamma} \tag{2.8}$$

It is important to underline that the contact angle's definition is unique as far as the solid substrate is ideal, and the drop is in static conditions. By contrast, on actual surfaces it is possible to define two further angles, setting a critical condition for the stability of the contact line: considering a water drop lying on a solid substrate, by inflating it the contact line does not immediately move, but the contact angle exceeds the value found in Equation 2.8. The contact line shifts after the contact angle overcomes a threshold value θ_A, called *advancing contact angle*. Analogously, if the drop is deflated, the angle reduces, and the contact line does not move until it goes down to the limit θ_R, called *receding contact angle*. The difference between the advancing and the receding angles, $\theta_A - \theta_R$, is defined as *hysteresis*, and it is involved in several capillarity phenomena. Finally, it is possible to specify a *sliding angle*, α, as the limit to incline the solid substrate before the contact line starts to shift. A schematic overview of
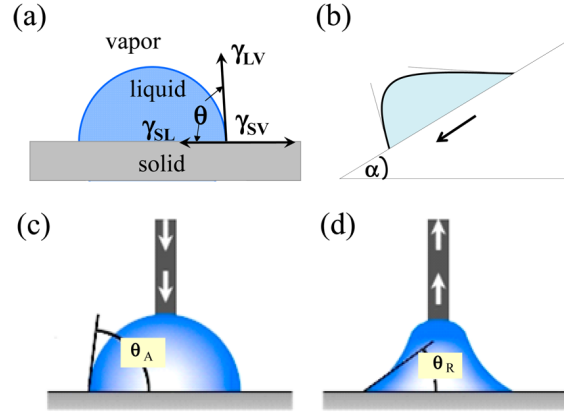
Figure 4: Overview of the various angles characterizing material wettability. Reprinted with permission from [1]. Copyright 2014 American Chemical Society.

the defined characterizing angles is given in Figure 4.

Contact angles are fundamental to classify the *wettability* of materials, namely their degree of wetting: a solid substrate can be defined *hydrophilic* or *hydrophobic* according to its affinity or lack of affinity for water. The scientific community sets the threshold to distinguish material wettability at $\theta_E = 90°$, and such definition is suitable for most applications. However, using the static contact angle might be misleading for more specific analyses, whereas the *receding* contact angles better defines the wettability threshold ($\theta_R = 90°$), as explained in [1].

2.4   Capillarity and gravity

It is remarkable that liquids may be unaffected by gravity effect, within certain well-defined conditions: for instance, fog is constituted of water droplets suspended in air, whose small size allows them to float. As a matter of fact, the dimension of the drop plays a main role in determining the effect of gravity on water.

In particular, it is possible to define a threshold below which gravity effects on water drops is negligible, called *capillary length*, κ^{-1}. If one considers a liquid subjected to gravitational field $g = -9.81 \, m/s^2$ and compares the Laplace pressure to the hydrostatic one, the following relation will be obtained:

$$\kappa^{-1} = \sqrt{\frac{\gamma}{\rho g}} \tag{2.9}$$

For example, water is characterized by $\kappa_{water}^{-1} \approx 2.7 \, mm$. Hence, when the size of a drop r is lower than the capillary length, capillarity effect prevails on gravity, making it negligible, otherwise, gravity counts.

It is possible to formulate such condition, defining a non-dimensional quantity comparing gravity forces with capillarity effects, called *Bond number*:

$$Bo = \frac{\Delta \rho \, g \, l^2}{\gamma} \tag{2.10}$$

where $\Delta \rho = \rho_l - \rho_v$ is the difference between the liquid and vapor phase (most of the times the latter is negligible with respect to the former) and l is a *characteristic length*, typical of the treated problem. For example, l might be the radius of a sphere with the same volume as the studied drop's size.

Furthermore, capillary length also defines the parts of the liquid that are subject to capillary effect and partially screened from gravity: for instance, by perturbing a liquid film, the effect can be observed only within a distance from the source equal to the capillary length. In wetting problems, this is the case of the so-called *heavy drops*: considering a water drop deposited on
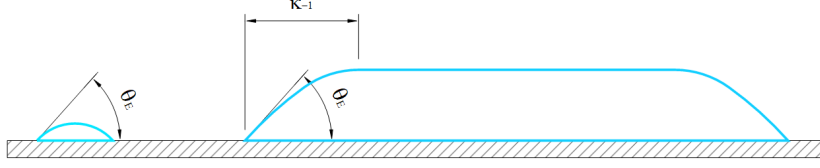
Figure 5: Comparison between a water droplet and a heavy drop. Capillary effect can be observed within κ^{-1} from the contact line.

a smooth surface, when its size is greater than the capillary length, gravity effect flattens the drop. However, a capillary length far from the contact line, the drop keeps its curved shape due to capillary effects (Figure 5). By contrast, if the water drop is smaller than κ^{-1}, effect of gravity can be neglected. Thus, droplets assume a spherical cap shape when lying on a smooth flat surface, as can be seen in Figure 5).

2.5 Wettability and roughness

In section 2.3, Young's relation for the equilibrium contact angle of a water drop on an ideal flat surface was given. However, research deals with real substrates, which might present inherent irregularities, as well as specifically designed textures and heterogeneity.

The relations analyzed so far do not apply to actual surfaces, as highlighted by Johnson and Dettre in 1964 [9]: in their research, they iteratively measured advancing and receding contact angles of water drops on a surface sequentially subjected to heat treatments to increase

its roughness. Their results showed that both the angles underwent considerable variation, generally increasing beyond a certain value of the roughness r, defined as follows:

$$r = \frac{A_{actual}}{A_{apparent}} \tag{2.11}$$

where A_{actual} is the real surface area and $A_{apparent}$ the apparent one, namely its projection on a plane parallel to the solid substrate. Hence, from such result it is noticeable that roughness considerably affects material wettability: consequently, a valid model to describe roughness influence is required, in order to understand this phenomenon.

Two models have been proposed to predict the evolution of wettability with material irregularities of physical and chemical nature, respectively. As so often in research, a combination of the two may lead to an optimal description of the phenomenon.

2.5.1   Wenzel's model

The first to systematically study roughness effect on wettability was Wenzel [9]. His model concentrates on physical irregularities, assuming that the material is chemically homogeneous. Furthermore, Wenzel hypothesized that locally the contact angle measured θ_E, namely the value obtained from Young's equation.

As can be seen in Figure 6, considering a drop deposited on a rough surface, the difference in surface energy per unit length after moving the contact line by an infinitesimal displacement dx can be calculated as:

$$dE = (\gamma_{ls} - \gamma_{vs}) \, r \, dx + \gamma cos\theta^* \, dx \tag{2.12}$$
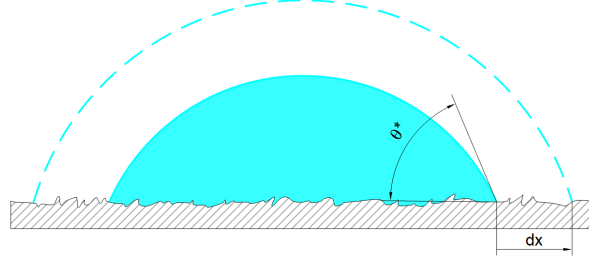
Figure 6: Scheme for Wenzel's contact angle derivation.

where θ^* is the apparent contact angle on the rough surface. Imposing the equilibrium condition $(dE = 0)$, one can obtain:

$$\gamma cos\theta^* = r\left(\gamma_{vs} - \gamma_{ls}\right) \tag{2.13}$$

$$cos\theta^* = r\,\frac{\gamma_{vs} - \gamma_{ls}}{\gamma} = r\,cos\theta_E \tag{2.14}$$

Equation 2.14 is known as Wenzel's relation and highlights how roughness increases wettability properties, both in the hydrophobic and in the hydrophilic case. As a matter of fact, according to Wenzel's relation:

$$\begin{cases} \theta_E < 90° \ \rightarrow \ \theta^* < \theta_E \\ \\ \theta_E > 90° \ \rightarrow \ \theta^* > \theta_E \end{cases} \tag{2.15}$$

Although Wenzel's model is assessed for several problems, its application is limited by its following doubtful consequence: according to it, it is possible to achieve complete wetting $(\theta^* = 0)$ by imposing the suitable roughness value $r_{limit} = \dfrac{1}{cos\theta_E}$. Such statement is not

consistent with actual observation, thus limiting Wenzel's application to cases with roughness much smaller than the size of the studied drop.

2.5.2 Cassie-Baxter model

Differently, Cassie and Baxter concentrated on planar surfaces with chemical heterogeneity, namely composed by different chemical species [10]. Considering a two-phase substrate, they computed the portions of liquid/solid interface occupied by each of the two species, characterized by their own Young's contact angles θ_1 and θ_2. Then, they evaluated the fractional surface area occupied by each of the species, namely:

$$\begin{cases} f_1 = \frac{A_1}{A_{tot}} \\[2mm] f_2 = \frac{A_2}{A_{tot}} \end{cases} \tag{2.16}$$

Hence, analogously to Wenzel's procedure, the difference in surface energy after a displacement dx of the contact line was computed, considering both the chemical species:

$$dE = f_1 \left(\gamma_{ls} - \gamma_{vs}\right)_1 dx + f_2 \left(\gamma_{ls} - \gamma_{vs}\right)_2 dx + \gamma \, cos\theta^* \, dx \tag{2.17}$$

Imposing the equilibrium condition ($dE = 0$), the following expression for the equilibrium contact angle was obtained:

$$cos\theta^* = f_1 \, cos\theta_{E_1} + f_2 \, cos\theta_{E_2} \tag{2.18}$$
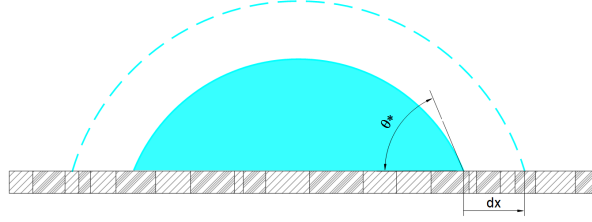
Figure 7: Scheme for Cassie-Baxter contact angle derivation.

In summary, Cassie-Baxter relation leads to the definition of relative surface tension between the liquid and solid phases as a weighted average of the relative surface tensions of two ideal systems, each with single phase solid substrates.

2.5.3   Hydrophilic composite rough surfaces

As mentioned in section 2.5, Wenzel's and Cassie-Baxter model can be integrated in order to obtain a more reliable representation of actual surface wetting [10]. As it will be seen, such combination allows to partially overcome Wenzel's limit of application to small scale roughness. When a liquid film spreads over a rough substrate, the grooves between the roughness tips are filled with water, creating a continuous flat liquid/solid patterned surface, as shown in Figure 8. It is possible to analyze such pattern as a chemical heterogeneity, defining the fractional surface area occupied by the solid phase $\Phi_s = \dfrac{A_{solid}}{A_{tot}}$, namely the area of the "island" emerging from the liquid.
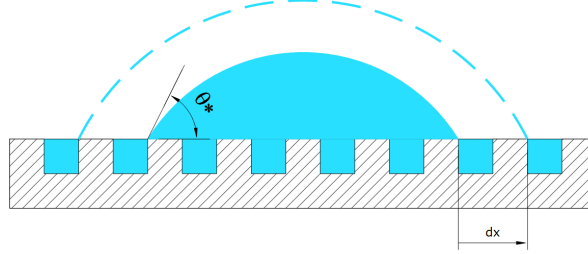
Figure 8: Scheme for the derivation of contact angle of a porous hydrophilic substrate through mixed Wenzel/Cassie-Baxter approach.

Hence, by applying Cassie-Baxter model to such equivalent system, with the null water/water contact angle $\theta_{E_{w/w}}$, one can obtain the expression for the contact angle θ^*:

$$cos\theta^* = 1 - \Phi_s + \Phi_s \, cos\theta_E \qquad (2.19)$$

It is remarkable to underline that such model can be used for penetrating liquid films on porous surfaces, consequently still leaving doubts about micro-textured surfaces analysis, whose roughness scale is comparable with the features one. However, it was important to explain it, in order to show how models can be related to improve their reliability.

To summarize, an overview of wetting phenomena was illustrated in this chapter, focusing the attention on the topics involved in the present study. With the theoretical background given so far, the study of equilibrium droplet shape on the analyzed beetle inspired micro-textured surface can be approached.
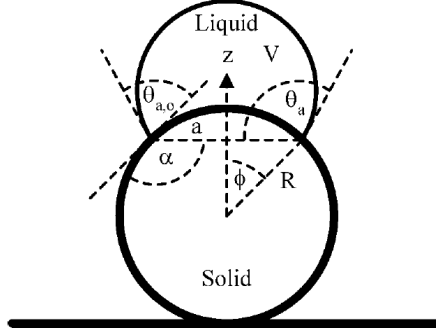
Figure 9: Schematic of a water droplet deposited on a spherical wall. Reprinted with permission from [2]. Copyright 2008 American Chemical Society.

2.6 Equilibrium contact angle measured on curved surfaces

All the solid substrates analyzed in the previous sections are characterized by a horizontal baseline. Contact angle measurement may be tricky when the studied droplet deposits over a curved surface. Particularly, in the present case study, the beetle's shell is curved, which introduces challenges when one wishes to study how droplets behave on non-flat surfaces. The shape assumed by water droplets depositing on curved walls was modeled by Extrand and Moon [2], who observed water droplets spreading on a spherical smooth substrate. The droplets were symmetrically centered on the spherical wall, as shown in Figure 9. From this scheme, it is possible to define several parameters, characterizing the geometric shape:

- *Intrinsic advancing contact angle*, $\theta_{a,o}$: contact angle expected for the same volume of liquid spreading on a flat surface;

- *Apparent advancing contact angle*, θ_a: contact angle measured with reference to the horizontal line intersecting the contact line.

- *Spreading angle*, ϕ: angle between the contact line and the vertical axis z;

- $2a$: the chord intersecting the contact line, perpendicular to axis z;

- R: the known radius of the spherical wall.

The intrinsic advancing contact angle $\theta_{a,o}$ is defined between the tangent line to the drop's spherical cap and the tangent line to the spherical wall. Its value could be calculated by combining the following relations, obtained from the geometry in Figure 9:

$$\theta_a = \theta_{a,o} + (\pi - \alpha) \tag{2.20}$$

$$\phi = arcsin\left(\frac{a}{R}\right) \tag{2.21}$$

$$\alpha = \pi - \phi \tag{2.22}$$

Hence, substituting Equation 2.21 and Equation 2.22 into Equation 2.20, the intrinsic advancing contact angle can be calculated as:

$$\theta_{a,o} = \theta_a - arcsin\left(\frac{a}{R}\right) \tag{2.23}$$

It is important to underline that Extrand and Moon developed the relations above reported for advancing contact angles. However, it is possible to perform the same analysis from the equilib-

rium contact angle point of view, obtaining the following relation for the intrinsic equilibrium contact angle:

$$\theta_{E,o} = \theta_E - arcsin\left(\frac{a}{R}\right) \tag{2.24}$$

Equation 2.24 will be particularly useful in the beetle's shell wettability assessment, as described in chapter 4.

CHAPTER 3

SE-FIT

The physics of interfacial phenomena is heavily correlated with minimum energy attainment, aka. *equilibrium* configuration. Particularly, in the present study the goal is to analyze and simulate water interaction on a surface in steady-state conditions: thus, it is logical to assume that the final shape of the water droplet will coincide with the equilibrium of the system, constituted by the liquid phase, the solid surface and their interface.

For this reason, the contact-line physics may be studied from the energy point of view, as minimization of energy of a body with an arbitrary initial configuration, but with the same physical characteristics as the investigated droplet, in particular, density ρ, surface tension γ, volume V and contact angle θ.

3.1   Surface Evolver

The energy minimization-based computation in this work is executed in *Surface Evolver* (SE), an interactive console program for the investigation of liquid surfaces. This open source software was developed by Professor Ken Brakke, Mathematics Department, Susquehanna University, Senlinsgrove, PA, and was initially included in the Minimal Surfaces Group of the Geometry Supercomputing Project (now The Geometry Center), sponsored by the National Science Foundation, the Department of Energy, Minnesota Technology, Inc., and the University of Minnesota.

In *Surface Evolver*, the user can accomplish simulations writing a datafile in portable C language. The software works by computing the shape and stability of equilibrium fluid interfaces: by defining a first surface, and imposing its boundary specific constraints for the case, the software will divide the obtained model into a triangular mesh, with settable refinement level. Then, SE evolves the surface toward the minimal energy condition by a gradient descent method, as described in section 3.3.5.

SE can be used in several fields of Physics and Engineering, particularly in applications where body forces are negligible with respect to surface forces (i.e. with low Bond numbers), such as Nanotechnology, micro-scale wicking structures, inkjet printing, Propellant Management Devices (PMD), micro-gravity tankage).

3.2   Surface Evolver - Fluid Interface Tool (SE-FIT)

Although the base principle of SE is pretty intuitive, writing the datafile and interfacing with the software is not trivial.

This reason persuaded the Capillary Fluidics Laboratory team from the Department of Mechanical and Materials Engineering at the Portland State University (PSU), Portland, OR, to develop a user-friendly Graphical User Interface (GUI), for *Surface Evolver*, leading to the conception of SE-FIT. The GUI makes SE easy and user-friendly.

Furthermore, while SE is written in ANSI C, as specified above, SE-FIT works with Microsoft Visual BASIC .Net. The communication between the GUI and Ken Brakke's software is possible, modifying the SE to support a file layer mode, where the input and the output go through text files, obtaining the new program *L Surface Evolver* (LSE).
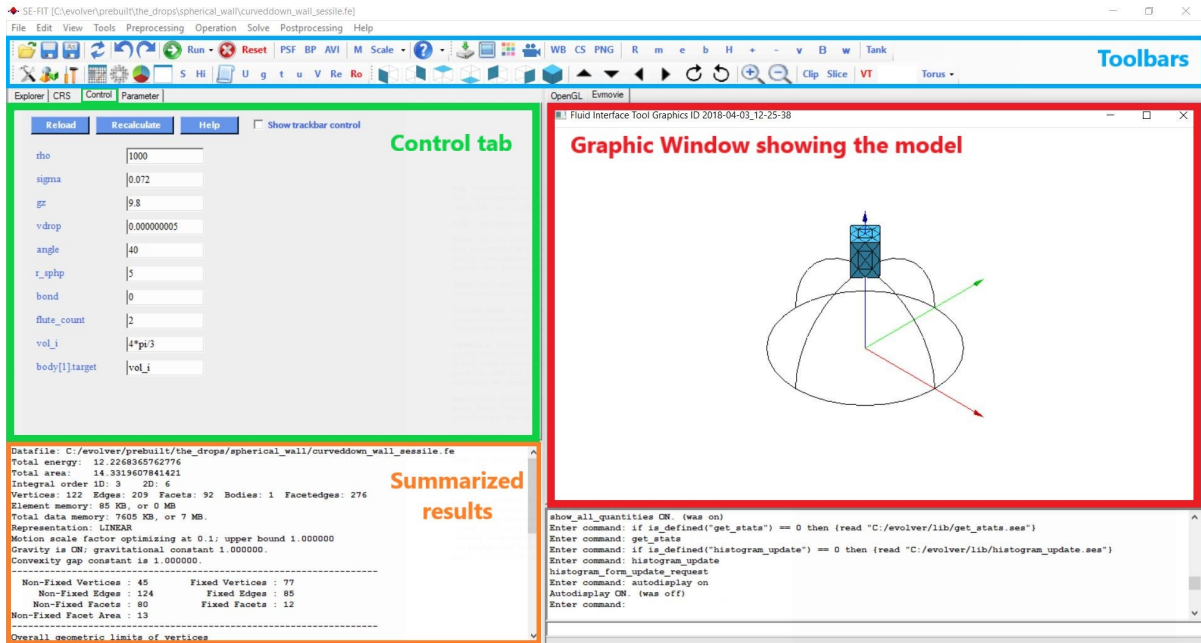
Figure 10: Screenshot of SE-FIT's interface with the described keys and windows highlighted.

The first instrument that SE-FIT provides for designing a simulation is the Text Editor, created with the purpose of editing and debugging the command stripts: here the user can specify all the necessary information for defining the liquid body's and the environment's geometries and constraints, the drop's physical characteristics, the gravity constant and how to compute the gravitational energy, and the coordinates of the body's center of mass.

Secondly, SE-FIT allows to keep constantly under control what is described in the Text Editor, showing the result in the Fluid Interface Tool Graphics. It is important to underline that if the script contains errors, after its execution, the program returns a message for the user, reporting the wrong line or the issue encountered by the compiler.

Certainly, SE-FIT's most important feature is the capability to control the simulation by a set of buttons: these can be classified into three categories:

- **Graphic window control**: clicking on the specific button, the user can either choose the type of view or rotate the model, as well as zoom in and out at one's own convenience. Moreover, SE-FIT allows to obtain a section of the model through button *Clip*, to better visualize the characteristics of the contact line, and to descern the detail of the drop's profile on the section plane, with the *Slice* command. Finally, it is possible to set the viewing parameters.

- **Simulation control**: the simulation can be managed either automatically or manually. The *Run* button consents to start the convergence with the default mesh settings: as suggested by the definitions, *Rough Convergence* uses a coarser discretization than *Fine Convergence*. By contrast, it is possible to conduct the convergence manually, one iteration at a time (button *g*) and refining or roughening the mesh at one's convenience (commands *Re* and *Ro*, respectively).

  The *Parameter Sweep Function* (PSF) can be considered one of the best contributions given to *SE*: with this function, the user can indeed execute the same simulation automatically changing the value of one or more parameters, recording the result variation into a *Comma-Separated Value* (CSV) file. If instead one only wants to observe how the configuration varies changing simply a parameter, the *Control* tab permits to modify this parameter in the specific boxes.

- **Output commands**: these functions allow the user to obtain results from SE-FIT, for example saving a PNG image file of a chosen view in the graphic window or exporting a 3D model of the converged drop, in several available file formats (e.g. ANSYS, DXF, IGES, STL).

3.3   Evaluation of Potential Energy in SE-FIT

As mentioned above, *Surface Evolver*'s goal is to lead the system to an equilibrium condition, evaluating the minimum of the potential energy. For most cases, the potential energy comprises interfacial surface energy, E_I, gravitational energy, E_G, and, rarely, rotational kinetic energy, E_R. Hence, the overall potential energy can be written as:

$$E = E_I + E_G + E_R \tag{3.1}$$

For each contribution, a mathematical definition will be searched, in order to collect the three parts and to have a global expression of the potential energy.

3.3.1   Interfacial Energy

Interfacial energy appears whenever a system shows a phase discontinuity. The surface separating the two phases, namely the interface, possesses a potential energy termed as interfacial energy. In wettability problems, this energy is proportional to the interface area between phases 1 and 2, A_{12}, according to the following law:

$$E_I = \gamma_{12}\, A_{12} \tag{3.2}$$
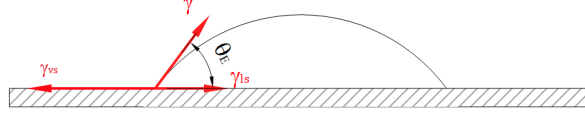
Figure 11: Diagram of a sessile drop in contact with a smooth planar surface: the surface tensions at the three interfaces and the equilibrium contact angle are outlined.

where the constant of proportionality γ_{12} is the surface tension between the two phases.

In the specific case of a drop laying on a solid surface, three interfaces appear, each one characterized by its interfacial energy, as can be seen in Figure 11. The interfacial surface energy of such system can be written as:

$$E_I = \gamma_{vs}\, A_{vs} + \gamma_{vl}\, A_{vl} + \gamma_{ls}\, A_{ls} \qquad (3.3)$$

where subscripts v, l and s stay for *vapor*, *liquid* and *solid*, respectively. Defining the total area of the solid phase as A_s, it is possible to state that:

$$A_{vs} = A_s - A_{ls} \qquad (3.4)$$

Hence, substituting Equation 3.4 into Equation 3.3, one can obtain:

$$E_I = \gamma_{vs}\, A_s + \gamma_{vl}\, A_{vl} + (\gamma_{ls} - \gamma_{vs})\, A_{ls} \qquad (3.5)$$

Since the first term of the right-hand side's contribution is much lower than the following sum, it can be neglected. Thus, remembering Young's relation in Equation 3.6, summarizing the force balance in Figure 11, and substituting it into Equation 3.5, the final Equation 3.7 is achieved:

$$\gamma_{vs} = \gamma_{ls} + \gamma_{vl} \, cos\theta \tag{3.6}$$

$$E_I = \gamma_{vl} \left(A_{vl} - A_{ls} \, cos\theta \right) \tag{3.7}$$

3.3.2   Gravitational Energy

With reference to the system shown in Figure 11, the attention is now focused on its gravitational energy evaluation. Considering a Cartesian reference frame centered in the solid phase's center of mass, the global gravitational energy is given by:

$$E_G = \rho_l \, V_l \, \vec{g} \cdot \vec{C}_l + \rho_v \, V_v \, \vec{g} \cdot \vec{C}_v \tag{3.8}$$

where:

- ρ_l, ρ_v are the densities of the liquid and vapor phases, respectively;

- V_l, V_v are the volumes of the liquid and vapor phases, respectively;

- $\vec{g}$ is the gravitational vector;

- $\vec{C}_l$, $\vec{C}_v$ are the displacement vectors linking the origin to the center of the liquid and vapor mass, respectively. Particularly, they can be expressed by calculating the Cartesian coordinates of the centers of mass, as follows:

$$\vec{C}_l = \frac{\int_{V_l} x\, dV}{V_l}\, \hat{i} + \frac{\int_{V_l} y\, dV}{V_l}\, \hat{j} + \frac{\int_{V_l} z\, dV}{V_l}\, \hat{k} \qquad (3.9)$$

$$\vec{C}_v = \frac{\int_{V_v} x\, dV}{V_v}\, \hat{i} + \frac{\int_{V_v} y\, dV}{V_v}\, \hat{j} + \frac{\int_{V_v} z\, dV}{V_v}\, \hat{k} \qquad (3.10)$$

Finally, remembering integrals' additive property and referring to the total volume V_t and to its center of mass' displacement vector $\vec{C}_t$, it is possible to state the following expression:

$$V_l\, \vec{C}_l + V_v\, \vec{C}_v = V_t\, \vec{C}_t \qquad (3.11)$$

Substituting $\rho_l = \rho_l + \rho_v - \rho_v$ and Equation 3.11 into Equation 3.8 and reorganizing the terms, one can obtain:

$$E_G = \rho_v\, \vec{g} \cdot (V_l\, \vec{C}_l + V_v\, \vec{C}_v) + (\rho_l - \rho_v)\, V_l\, \vec{g} \cdot \vec{C}_l =$$

$$= \rho_v\, V_t \vec{g} \cdot \vec{C}_t + (\rho_l - \rho_v)\, V_l\, \vec{g} \cdot \vec{C}_l \qquad (3.12)$$

Hence, since the centroid of the total volume is fixed, the product $V_t \vec{C}_t$ is constant: as a consequence, the definition of the gravitational potential energy is valid even if it is omitted. Eventually, this leads to the following final expression for the gravitational potential energy:

$$E_G = (\rho_l - \rho_v) V_l \, \vec{g} \cdot \vec{C}_l \tag{3.13}$$

Eventually, it is important to underline that the density of the vapor phase ρ_v, which in our case is represented by air ($\rho_{air} = 1.2 \, kg/m^3$, for $p = 1 \, atm$ and $T = 20°C$), is very small, compared to the density of water ($\rho_{water} = 1000 \, kg/m^3$). Thus, it is possible to rewrite Equation 3.13 as follows:

$$E_G = \rho_l \, V_l \, \vec{g} \cdot \vec{C}_l \tag{3.14}$$

3.3.3 Rotational Kinetic Energy

The rotational kinetic energy can be calculated for a generic system as:

$$E_R = \frac{1}{2} \, \vec{\omega}^T \, \mathbf{I} \, \vec{\omega} \tag{3.15}$$

where:

- $\vec{\omega}$ is the angular velocity vector;

- $\mathbf{I}$ is the moment of inertia tensor, evaluated for the complete system liquid/vapor.

However, since the present case copes with a sessile droplet interacting with a fixed surface in steady condition, one has that

$$\vec{\omega} = \vec{0} \tag{3.16}$$

Thus, the rotational kinetic energy for this case of study can be considered null:

$$E_R = 0 \tag{3.17}$$

In conclusion, our case of study is characterized by two potential energy contributions, neglecting the rotational component. Grouping together Equation 3.7, Equation 3.14, and Equation 3.17, one can obtain the following expression:

$$E_P = E_I + E_G + E_R = \gamma_{vl} \left(A_{vl} - A_{ls} \, cos\theta \right) + \rho_l \, V_l \, \vec{g} \cdot \vec{C_l} + 0 \tag{3.18}$$

3.3.4   Dimensionless Form of Potential Energy

Surface Evolver converges the system defined in the script (see section 3.4) towards the equilibrium condition. As explained in [9], this condition is given by:

$$\delta W = \delta E_P = 0 \tag{3.19}$$

where δW is the elementary work executed by all the external forces acting on the system, coinciding with the variation of its potential energy. Thus, a system is in equilibrium when it reaches the minimum potential energy condition.

As it will be illustrated in section 3.4, SE identifies a droplet as a *body*, comprising its faces, edges and vertices. Like every computational software, SE divides the drop's body into a triangular mesh, individuating many points on its faces. For each point m of the mesh, SE calculates the potential energy E_{Pm}, evaluating then an acting force $\vec{F_m}$:

$$\vec{F_m} = -\nabla E_{Pm}|_{x,y,z} \tag{3.20}$$

This vector determines a displacement of point m during the considered iteration, so that the whole system evolves towards a new condition. The described process is repeated at each iteration, until SE detects that every point m satisfies the condition $F_m = 0$ (i.e. the system solution converged).

Once the mathematical expression for potential energy has been achieved (Equation 3.18), some considerations ought to be made: if SE used this very expression for its calculation, the convergence operations would be extremely time-consuming and inefficient. For this reason, an elaboration of Equation 3.18 is required, with the aim of making SE's action lighter and computationally cheaper. Hence, referring to [11], potential energy is expressed in a reduced order differentiable form.

First, it is useful to scale the involved quantities with respect to the liquid/vapor surface tension, as shown in Equation 3.21: in this manner, the simulations executed on SE will apply for any

fluid (i.e. for every value of surface tension). Consequently, the default surface tension will be unitary.

$$\frac{E_P}{\gamma_{vl}} = (A_{vl} - A_{ls}\,cos\theta) + \frac{\rho_l\,|\vec{g}|}{\gamma_{vl}}\,V_l\,\frac{\vec{g}}{|\vec{g}|}\cdot\vec{C}_l \tag{3.21}$$

Secondly, it is worthwhile to express Equation 3.21 in a dimensionless form: for this purpose, a *characteristic length* L must be defined, for instance, the radius of a spherical droplet with the same volume as the one studied:

$$L = \left(\frac{3\,V_l}{4\,\pi}\right)^{\frac{1}{3}} \tag{3.22}$$

After some manipulations, one obtains the dimensionless form of the potential energy, E_P^*:

$$E_P^* = \frac{E_P}{\gamma_{vl}\,L^2} = \frac{A_{vl} - A_{ls}\,cos\theta}{L^2} - Bo\,\frac{V_l}{L^4}\,\frac{\vec{g}}{|\vec{g}|}\cdot\vec{C}_l \tag{3.23}$$

$$Bo = \frac{\rho_l\,|\vec{g}|\,L^2}{\gamma_{vl}} \tag{3.24}$$

where Equation 3.24 defines the Bond number, namely the ratio between the gravitational and capillarity forces.

In conclusion, Equation 3.23 is the reduced form of the potential energy and was derived to reduce the computational requirements.

3.3.5   Minimization of the Potential Energy: the Gradient Descent Method

In order to accomplish convergence to the equilibrium condition, *Surface Evolver* applies the Gradient Descent algorithm. The Gradient Descent is an approximative method to solve algebraic linear systems [12]: it is based on the observation that a multi-variable function $F(\vec{x})$,

defined and differentiable in a neighborhood of a point $\vec{a}$, decreases fastest for neighboring points in the direction of $-\nabla F(\vec{a})$. Consequently, it is possible to calculate the coordinates of such points as a function of the gradient of $F(\vec{a})$ [13].

For instance, considering a point $\vec{a_n}$, with known $F(\vec{a}_n)$, it is possible to compute a new neighboring point $\vec{a}_{n+1}$ such that:

$$F(\vec{a}_{n+1}) \leq F(\vec{a}_n) \tag{3.25}$$

where:

$$\vec{a}_{n+1} = \vec{a}_n - \gamma \, \nabla F(\vec{a}_n) \tag{3.26}$$

In Equation 3.26, γ is defined as the *step size*, namely a scale factor calculated specifically for each case study. The method starts guessing an arbitrary point $\vec{x}_0$ as a local minimum, calculating the value of the function there. Hence, it computes $\nabla F(\vec{x}_0)$ and the following point $\vec{x}_1$ using Equation 3.26. This operation is repeated iteratively N times, until $F(\vec{x}_N)$ reaches a value small enough indicating convergence.

Analogously, taking under consideration the present problem, the studied function is the potential energy $E_P(\vec{x})$, simultaneously calculated in the different nodes of the mesh, according to Equation 3.23. For each point P, the algorithm computes the value of the potential energy

in the initial position of P, $\vec{x}_0^{(P)}$. Then, Equation 3.26 is applied for the first iteration, and the value of the potential energy in the new obtained point $\vec{x}_1^{(P)}$ is calculated, as follows:

$$\vec{x}_1^{(P)} = \vec{x}_0^{(P)} - \gamma_0 \, \nabla E_P(\vec{x}_0^{(P)})$$

$$E_P(\vec{x}_1^{(P)}) \le E_P(\vec{x}_0^{(P)})$$

As one would expect, the value of the function at the first iteration never satisfies the desired condition: consequently, this procedure must be repeated until convergence is obtained. Particularly, at each iteration n, one has:

$$\vec{x}_{n+1}^{(P)} = \vec{x}_n^{(P)} - \gamma_n \, \nabla E_P(\vec{x}_n^{(P)})$$

$$E_P(\vec{x}_{n+1}^{(P)}) \le E_P(\vec{x}_n^{(P)})$$

Eventually, the convergence is reached for the N-th value calculated $E_P(\vec{x}_N^{(P)})$, such that:

$$E_P(\vec{x}_N^{(P)}) \le E_P(\vec{x}_{N-1}^{(P)}) \le \cdots \le E_P(\vec{x}_1^{(P)}) \le E_P(\vec{x}_0^{(P)})$$

3.4   The *Facet-Edge* (*.fe*) file: composition of the script

The simulations' scripts are contained in *Facet-Edge* files (*.fe*), an extension specifically invented by Brakke. They can be opened and managed by the SE-FIT's Text Editor, where they appear as text documents, showing highlighted keywords .

In order to achieve a complete and reliable simulation, it is necessary to follow a precise path,

each step of which corresponds to the definition of a physical or geometrical quantity of the studied problem, outlining the initial configuration of the surface in an ASCII datafile. Then, it will be read by a lexical analyzer, interpreting the prescribed information.

The following sections report the series of parts constituting the script, required for the analysis.

3.4.1   Parameters and macros

Surface Evolver allows the user to define the geometrical and physical quantities of the problem through two types of variables, each one with specific characteristics. Firstly, a value can be attributed to a variable by defining a *parameter* through the following code line:

```
PARAMETER identifier constant_value
```

where *identifier* can be any string without a special meaning to the parser. Everytime the identifier is cited in the script, it will be interpreted as the *constant_value* assigned. The main advantage taken by this type of definition is the possibility to change the value of a parameter after the simulation is run in the *Control* tab. In this manner, SE will recalculate the equilibrium condition, taking as initial state the previously converged system. This procedure can be useful in wettability analysis, for example when the user is interested in measuring the advancing or receding contact angle: by increasing and decreasing the volume of the investigated drop, addition and subtraction of liquid can be simulated, reproducing suction experiments.

On the contrary, whenever a user wants to set a variable as a function of multiple parameters, it is possible to define a *macro*, through the following code line:

```
#define identifier (string)
```

where *string* indicates any sequence of characters resulting in a mathematical operation between the involved parameters. Also in this case, whenever the analyzer finds the prescribed identifier, it will interpret it as the assigned string.

Typically, physical quantities, such as density, volume, gravitational constant, surface tension and contact angle, and the main geometrical dimensions of both the wall and the drop are defined as parameters, so that one can observe the equilibrium condition varying as their function. On the other hand, quantities derived from the assigned parameters can be defined as macros through mathematical operations.

3.4.2 <u>Environmental Conditions</u>

The following part of the script must contain information about the environmental conditions, deriving from the previously defined physical quantities. First of all, the characteristic length of the droplet and the *Bond number* are calculated according to their mathematical definition (see Equation 3.24 for Bond number), defining them as macros. Particularly, one has:

```
#define  l_char  ((3*vol/4/pi)^(1/3))
#define  Bond_number  ((rho*gz*l_char^2)/sigma)
```

Secondly, the cosine of the contact angle, namely the relative surface tension on the wet wall (thus called *WALLT*), is computed:

```
#define  WALLT    (−cos(angle*pi/180))
```

It is important to underline that in order to investigate the potential energy, *Surface Evolver* will have to solve discretized volume and surface integrals over the fluid body: both the Bond number and the relative surface tension will be necessary for these calculations.

3.4.3   Gravitational Energy Evaluation

In this section of the script, the goal is to instruct *Surface Evolver* on how to calculate the gravitational potential energy of the liquid volume. According to the used reference frame, with $\vec{g} = -9.81\,m/s^2\,\vec{k}$, from the definition of the gravitational energy for a volume of fluid V, one has:

$$E_G = \int_V \rho\,g\,z\,dV = \rho\,g \int_V \nabla \cdot \left(\frac{z^2}{2}\vec{k}\right) dV \tag{3.27}$$

Applying the divergence theorem, it is possible to transform the volume integral on the fluid's body into a surface integral on its boundary. Then, discretizing the integral for each triangle i of the computational mesh, it is possible to write:

$$E_G = \frac{1}{2}\rho\,g \int_{\partial V} z^2\,dxdy \approx \frac{1}{2}\,\rho\,g \sum_{i=1}^{N}(z_i{}^2\,A_i) \tag{3.28}$$

This definition can be realized in SE by defining a *quantity*, namely the result of the summation of a certain value calculated for each triangular facet of the mesh. For a proper execution of the integral, it is necessary to assign such quantity to any face forming the free surface (i.e. the integration domain).

```
quantity grav_energy energy method facet_vector_integral
vector_integrand:
```

q1 : 0

q2 : 0

q3 : 1/2∗rho∗gz∗z^2

where *grav_energy* is a user-defined name. The method *facet_vector_integral* refers to:

$$\int_{\partial V} q_1 \, dydz + \int_{\partial V} q_2 \, dxdz + \int_{\partial V} q_3 \, dxdy \tag{3.29}$$

where q_1 and q_2 are null.

3.4.4   Center of mass calculation

Analogously to the process for the gravitational energy computation, it is possible to evaluate the coordinates of the center of the fluid mass as *quantities*. From their definitions, through the divergence theorem and further mathematical manipulations, one obtains:

$$x_{mc} = \frac{\int_V x \, dV}{V} = \frac{\int_{\partial V} zx \, dxdy}{V} \tag{3.30}$$

$$y_{mc} = \frac{\int_V y \, dV}{V} = \frac{\int_{\partial V} zy \, dxdy}{V} \tag{3.31}$$

$$z_{mc} = \frac{\int_V z \, dV}{V} = \frac{\int_{\partial V} \frac{z^2}{2} \, dxdy}{V} \tag{3.32}$$

By way of example, the demonstration of Equation 3.30 follows. Equation 3.31 and Equation 3.32 can be derived analogously:

$$x_{mc} = \frac{\int_V x \cdot 1 \, dV}{V} = \frac{\int_V x \left(\nabla \cdot (z\vec{k}) \right) dV}{V} = \frac{\int_V \nabla \cdot (xz\vec{k}) \, dV}{V} = \frac{\int_{\partial V} xz\vec{k} \cdot \vec{k} \, dx \, dy}{V} = \frac{\int_{\partial V} zx \, dxdy}{V}$$

Such calculated integrals can be implemented on *Surface Evolver* by defining the following *quantities*, applying them to the faces constituting the liquid free surface:

```
/* CENTER OF MASS DEFINITION */

quantity XMC info_only method facet_vector_integral

vector_integrand:

q1: 0

q2: 0

q3: z*x

quantity YMC info_only method facet_vector_integral

vector_integrand:

q1: 0

q2: 0

q3: z*y

quantity ZMC info_only method facet_vector_integral

vector_integrand:

q1: 0
```

```
q2 :  0

q3 :  1/2∗z^2
```

3.4.5   Definition of the constraints

As explained in sections 3.4.1 to 3.4.4, the first fractions of the code cope with the physical

parameters governing the problem, although no quantity related to the structure of the inves-

tigated system has still been defined, except for the geometric parameters and macros. As a

matter of fact, in *Surface Evolver* geometric entities must be defined as *constraints*, namely

solid figures described by their mathematical equations in the 3D Cartesian space. Undoubt-

edly, the constraints' characterization is the thorniest part of the script: to begin with, much

attention must be paid when expressing the geometric equations, in order to select the right

points in space. Additionally, constraints are related to the integrating operations performed

by the program to calculate the fluid's volume, the water/air interface area and the wet wall's

contribution to the gravitational energy.

The following code lines briefly mention how to geometrically set a constraint, as reported in

[14]:

```
constraint  c_name

formula :  F( x , y , z )  =  0
```

where *c_name* is an identifier that will denote the constraint and the *formula* in the second line

expresses the geometry.

Before deeply examining how constraints are defined, it is indispensable to mention how SE

executes such integrations: as it is described in section 3.4.3, the software can discretize surface

integrals (see Equation 3.28), not volume ones, though. Therefore, all the quantities mentioned

so far, physically defined as volume integrals, require to be transformed into surface integrations.

It is natural to accomplish this duty through *Gauss' theorem*, illustrated in [15]: also known as

the *divergence theorem*, it states that given a set $\Omega \subset \mathbb{R}^3$ and with $\vec{n}$ being the unit vector normal

to the boundary of Ω, $\partial\Omega$, the following relation is valid for all the vector fields $\vec{f} \in (\mathcal{C}^1(\bar{\Omega}))^3$

(i.e. first order differentiable on Ω and its boundary):

$$\int_\Omega \nabla \cdot \vec{f} \, dxdydz = \int_{\partial\Omega} \vec{f} \cdot \vec{n} \, d\sigma \qquad (3.33)$$

The second fundamental result in order to achieve the integral computation is *Stokes' theorem*,

presented in [15]: it asserts that given a cap surface $\Sigma \subset \mathbb{R}^3$, for which the unit vector $\vec{n}$

establishes a crossing sense and, correspondingly, a travel direction on the cap's boundary $\partial\Sigma$,

for all the vector fields $\vec{f} \in (\mathcal{C}^1(\bar{\Omega}))^3$ defined on an open set $A \subseteq \mathbb{R}^3$ containing Σ, the following

expression is valid:

$$\int_\Sigma (\nabla \times \vec{f}) \cdot \vec{n} \, dS = \oint_{\partial\Sigma} \vec{f} \cdot d\vec{l} \qquad (3.34)$$

In other words, the flux of the curl of $\vec{f}$ across the surface Σ corresponds to the circulation of

$\vec{f}$ on the boundary $\partial\Sigma$ of the surface. This relation is very useful when a surface integral needs

to be transformed into a line integral. Particularly, when it is applied to two-dimensional cases,

it reduces to *Green's theorem*(Equation 3.36), valid for all the vector fields $\vec{w}$, such that:

$$\vec{w}(x, y) = M(x, y)\, \vec{i} + N(x, y)\, \vec{j} \tag{3.35}$$

$$\int_{\Sigma} (\nabla \times \vec{w}) \cdot \vec{n}\, dS = \int_{\Sigma} \left(\frac{\partial N}{\partial x} - \frac{\partial M}{\partial y} \right) \vec{k} \cdot \vec{n}\, dS = \int_{\partial \Sigma} \vec{w} \cdot \vec{dl} \tag{3.36}$$

The mathematical theorems described allow SE to manage integrals, especially on faces which

are omitted due to computational reasons: such circumstance occurs with the liquid/solid

interface. As a matter of fact, if the wet wall was defined as a face, the mesh nodes belonging

to it would be subjected to a null displacement, as explained in [14]. As a result, the interface

would be fixed, compromising the simulation's result. Conversely, by omitting the liquid/solid

interface and constraining its edges to belong to the wet wall, it is possible to avoid this issue:

in addition, in order to compensate for the energy contribution missing from the interface

(namely to the body's volume, to the surface energy, and to the gravitational energy), its edges

are characterized by specific energy integrands, calculated through the cited theorems. The

following paragraphs explain how such integrands can be achieved.

First of all, it is worthwhile to analyze how *Surface Evolver* evaluates the **fluid body**

volume, V, namely:

$$V = \int_{B} dx dy dz \tag{3.37}$$

where B is the fluid body. The inability of SE to compute volume integral, compels to elaborate Equation 3.37 through Gauss' theorem as follows:

$$V = \int_B 1\, dxdydz = \int_B \nabla \cdot (z\vec{k})\, dxdydz = \int_{\partial B} z\vec{k} \cdot \vec{n}\, dA \qquad (3.38)$$

where $z\vec{k}$ is a vector field, such that $\nabla \cdot (z\vec{k}) = 1$, and ∂B is the boundary surface of B. Apparently, it would be enough to calculate such integral on every facet of the liquid volume's boundary. However, the solid/liquid interface is not programmed, since its presence would compromise the convergence operation. Therefore, all the facets only form part of ∂B. Nevertheless, thanks to integrals' additivity property, it is possible to split the integration domain into $\partial B = \partial B_{lv} \cup \partial B_{ls}$ (i.e. free liquid/vapor and liquid/solid interface, respectively), leading to the following expression:

$$V = \int_{\partial B_{lv}} z\vec{k} \cdot \vec{n}\, dA + \int_{\partial B_{ls}} z\vec{k} \cdot \vec{n}\, dA \qquad (3.39)$$

where the first integral is calculable by SE, while the second one still needs some elaborations. It is possible to solve analytically the integral over the liquid/solid interface, recurring to the definition of the constraint containing ∂B_{ls}. As a matter of fact, one has:

$$F(x, y, z) = 0 \iff z = f(x, y) \qquad (3.40)$$

Hence,

$$\int_{\partial B_{ls}} z\vec{k} \cdot \vec{n}\, dA = \int_{\partial B_{ls}} f(x,y)\, \vec{k} \cdot \vec{n}\, dA \qquad (3.41)$$

Thus, by considering the projection of ∂B_{ls} onto the $x - y$ plane, S_{xy}, applying Green's theorem

(Equation 3.36) to the two-dimensional case and reminding the definition of the suitable vector

field $\vec{w}$ (Equation 3.35), it is possible to write:

$$\int_{S_{xy}} f(x,y)\, \vec{k} \cdot \vec{n}\, dxdy = \int_{S_{xy}} f(x,y)\, dxdy = \int_{\partial S_{xy}} \vec{w} \cdot \vec{dl} \qquad (3.42)$$

with

$$f(x,y) = \nabla \times \vec{w} = \nabla \times (M(x,y)\,\vec{i} + N(x,y)\,\vec{j}) = \frac{\partial N}{\partial x} - \frac{\partial M}{\partial y} \qquad (3.43)$$

By solving the Ordinary Differential Equation 3.43 (ODE), the integrand to assign to the

considered constraint is obtained. For instance, one solution can be:

$$\begin{cases} M(x,y) = 0 \\[2ex] N(x,y) = \int f(x,y)\, dx \end{cases} \qquad (3.44)$$

Hence,

$$\vec{w}_{volume}(x,y) = M(x,y)\,\vec{i} + N(x,y)\,\vec{j} = \int f(x,y)\, dx\,\vec{j} = w_{yc}\,\vec{j} \qquad (3.45)$$

Next, the **wet wall surface area** needs to be evaluated, in order to impose the contact

angle specified in the first portion of the code (3.4.1). The liquid/solid interface S_{ls} is given by

the surface integral on the wet wall, which is not defined, though. Hence, recurring to Stokes' theorem:

$$S_{ls} = \int_{S_{ls}} dS = \int_{S_{ls}} (\nabla \times \vec{w}) \cdot \vec{n} \, dS = \int_{\partial S_{ls}} \vec{w} \cdot d\vec{l} \tag{3.46}$$

It is possible to define a suitable $\vec{w}$ by referring to the projection of S_{ls} on the $x - y$ plane, S_{xy}, through the method followed for the volume contribution. Conveniently, the function $z = f(x, y)$ can be utilized:

$$\nabla \times \vec{w} = \sqrt{1 + \left(\frac{\partial f}{\partial x}\right)^2 + \left(\frac{\partial f}{\partial y}\right)^2} \, \vec{k} \tag{3.47}$$

Leading to:

$$S_{ls} = \int_{S_{xy}} \sqrt{1 + \left(\frac{\partial f}{\partial x}\right)^2 + \left(\frac{\partial f}{\partial y}\right)^2} \, dxdy = \int_{\partial S_{xy}} \vec{w} \cdot d\vec{l} \tag{3.48}$$

By applying Green's theorem (Equation 3.36) the following ODE is found, leading to a possible solution shown in Equation 3.51:

$$\frac{\partial N}{\partial x} - \frac{\partial M}{\partial y} = \sqrt{1 + \left(\frac{\partial f}{\partial x}\right)^2 + \left(\frac{\partial f}{\partial y}\right)^2} \tag{3.49}$$

$$\begin{cases} M(x, y) = 0 \\ N(x, y) = \int \sqrt{1 + \left(\frac{\partial f}{\partial x}\right)^2 + \left(\frac{\partial f}{\partial y}\right)^2} \, dx \end{cases} \tag{3.50}$$
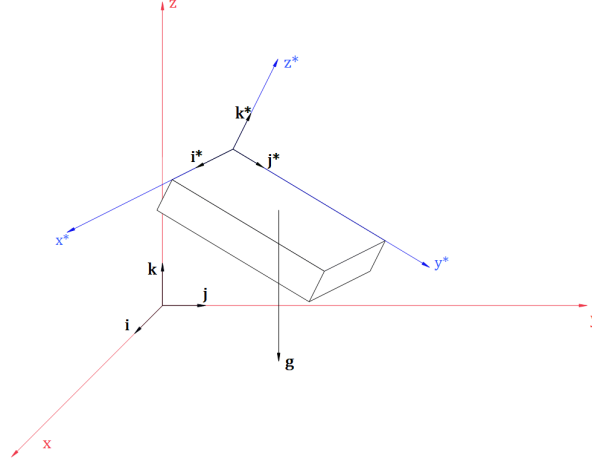
Figure 12: Inclined surface in the 3D space, described by two reference frames: global xyz and local $x^*y^*z^*$.

Hence,

$$\vec{w}_{surface}(x, y) = M(x, y)\,\vec{i} + N(x, y)\,\vec{j} = \int \sqrt{1 + \left(\frac{\partial f}{\partial x}\right)^2 + \left(\frac{\partial f}{\partial y}\right)^2}\, dx\vec{j} = w_{ye}\,\vec{j} \qquad (3.51)$$

Finally, the integral for the **gravitational energy** contribution of the wet wall must be set up, with reference to the chosen reference frame: as a matter of fact, the direction of the gravitational acceleration $\vec{g}$ may not coincide with one of the axes, for example when one is interested in studying an inclined surface. In such case, it could be useful to define a local wet wall based reference frame $x^*y^*z^*$, rototranslated with respect to the global frame xyz. With reference to Figure 12, the gravitational acceleration may be defined by:

$$\vec{g} = -|\vec{g}|\,\vec{k} = g_{x^*}\,\vec{i}^* + g_{y^*}\,\vec{j}^* + g_{z^*}\,\vec{k}^* \qquad (3.52)$$

According to the local reference frame, the gravitational energy components can be computed from the center of mass coordinates (Equation 3.30, Equation 3.31, Equation 3.32), substituting $z = f(x, y)$, as follows:

$$E_{gx^*} = -\rho g_{x^*} \int_{S_{x^* y^*}} x^* f(x^*, y^*) \, dx^* dy^* \tag{3.53}$$

$$E_{gy^*} = -\rho g_{y^*} \int_{S_{x^* y^*}} y^* f(x^*, y^*) \, dx^* dy^* \tag{3.54}$$

$$E_{gz^*} = -\rho g_{z^*} \int_{S_{x^* y^*}} \frac{1}{2} f^2(x^*, y^*) \, dx^* dy^* \tag{3.55}$$

However, for the present case study the global reference frame was conveniently used, determining:

$$\vec{g} = -|\vec{g}| \, \vec{k} = -9.81 \, m/s^2 \, \vec{k} \tag{3.56}$$

$$\begin{cases} E_{gx} = 0 \\[2mm] E_{gy} = 0 \\[2mm] E_{gz} = -\rho g_z \int_{S_{xy}} \frac{1}{2} f^2(x, y) \, dxdy \end{cases} \tag{3.57}$$

Analogously to the volume contribution calculation, it is possible to apply Green's theorem, leading to the following ODE:

$$\frac{\partial N_{gz}}{\partial x} - \frac{\partial M_{gz}}{\partial y} = \frac{1}{2} f^2(x, y) \tag{3.58}$$

Eventually, one obtains the following solution for Equation 3.58:

$$\begin{cases} M(x,y) = 0 \\ N(x,y) = \displaystyle\int \frac{1}{2} f^2(x,y)\, dx \end{cases} \tag{3.59}$$

Hence,

$$\vec{w}_{grav}(x,y) = M(x,y)\,\vec{i} + N(x,y)\,\vec{j} = \int \frac{1}{2} f^2(x,y)\, dx\vec{j} = w_{yg}\,\vec{j} \tag{3.60}$$

In conclusion, taking under consideration both the energy and the volume contributions, one can define each constraint, solving the integrals in Equation 3.45, Equation 3.51 and Equation 3.60 and substituting the solutions in the following code lines:

```
constraint  c_name

formula:  F(x,y,z)  =  0

energy:

e1:  0

e2:  −cos(theta)*w_y_e  −  gstuff_z

e3:  0

content:

c1:  0

c2:  −vstuff

c3:  0
```

where *vstuff*, *w_y_e*, and *gstuff_z* are the identifiers for Equation 3.45, Equation 3.51, and Equation 3.60, respectively.

3.4.6   Vertices, edges, faces and body

Once defining the constraints, the analyzed surface and the fluid mass must be drawn in the 3D space. This can be accomplished through the definition of geometric elements, that are organized in the following dimensional hierarchy in *Surface Evolver*:

- **Vertices**: dimensionless points, defined through their coordinates in the Cartesian 3D space. Characterized by the constraint(s) on which they lay, they can be either *fixed*, if part of the wall, or unfixed, if belonging to the liquid body. The following syntax is used for their declaration:

  ```
  n_vertex coord_1 coord_2 coord_3 constraint c_1 c_2 fixed
  ```

  where *n_vertex* is its identifying number. The attributes following the three coordinates are present only when the vertex belongs to a constraint and it is fixed, respectively, otherwise they are not defined;

- **Edges**: a line linking two vertices. It might be linear or, if belonging to a curved constraint, it may follow its curved boundary. Also edges can be either fixed or unfixed, depending on the presence of the attribute *fixed* in the defining line:

  ```
  n_edge vertex_1 vertex_2 constraint c_1 fixed
  ```

- **Faces**: a surface defined by three or more edges. Generally, only the faces of the liquid body are defined, attributing them the quantities set to calculate the gravitational energy

and the center of mass' coordinates, as well as a color to distinguish them from the wall, as follows:

```
n_face  edge_1  edge_2  edge_3  grav_energy  XMC YMC ZMC  color  blue
```

- **Body**: a 3D solid figure, defined through its faces. Its main attributes are the *volume*, namely the target volume that the program will seek for the convergence, and the *density*, the value involved in the gravitational energy computation.

As a final point, the very last section of the script contains some commands to apply to the described system, in order to prepare it for the convergence operations: first of all, the constrained edges are refined to be shown coherently with the constraint (e.g. curved edges). Secondly, if needed, the mesh refinement can be customized, according to the precision required by the analysis.

Having illustrated how to compose the script, the next step will be its application to the studied problem, concerning many delicate steps that must be considered.

CHAPTER 4

COMPUTATION RESULTS

The geometry of the SE-FIT simulation is expected to resemble closely to the actual beetle back shell (aka. elytron). Micrographs were obtained in Scanning Electron Microscope (SEM) setup using $2 \times 2 mm^2$ samples of dead beetle elytron, which can be seen in Figure 13. It is noticeable that the shell presents a characteristic roughness, due to the presence of approximately truncated spherical *bumps*, separated by sharp *valleys*. Measurements from SEM images show the diameter of the bumps to be $10\,\mu m$ and profilometric analysis provide elevations of the bumps to be approximately $2.5\,\mu m$. The valleys between them look more similar to grooves: as a matter of fact, the bumps can be considered as elevations, touching one another at their base. Additionally, the wettability of the beetles' curved elytron was analyzed through the approach described in section 2.6: water droplets were deposited on the shell and images of their shape were captured by a camera. Hence, such images were further processed, obtaining the apparent contact angle and the intrinsic equilibrium contact angle θ_E, through Equation 2.24. Thus, an equilibrium contact angle θ_E of approximately 70° was found, confirming information from literature about the beetles' elytron hydrophilicity [16].

4.1 Modeling the wet wall

Observing Figure 13, it is possible to individuate a regular pattern in the alternating elevations' rows: bumps look patterned in such a way that each one borders with other six of them,
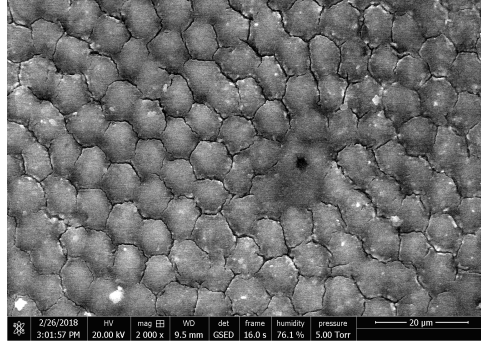
Figure 13: SEM image of the beetle's elytron micro-texture: alternating rows of bumps can be distinguished, forming an approximately hexagonal distribution.

hexagonally distributed around it. Assuming that all the bumps measure the same diameter of $10\,\mu m$ diameter, one can model the shell's morphology as a linear repetition of the hexagonal unit cell shown in Figure 14. As can be seen, an additional small $1\,\mu m$ distance was inserted between the bumps, in order to avoid singularities in the computation. As a matter of fact, if the bumps were in contact in a single point, the liquid surface in between could not be discretized: this would determine inconsistencies in the results, with the prediction of an incorrect behavior of the liquid surface between the bumps.

Once defined the unit cell of the model, the overall size of the wet wall must be defined, namely the number of unit cell linearly patterned. This can be chosen as a compromise between a measure large enough for the borders not to interfere with the convergence and a dimension small enough to neglect the shell's curvature. By considering a series of 9×9 bump rows, the
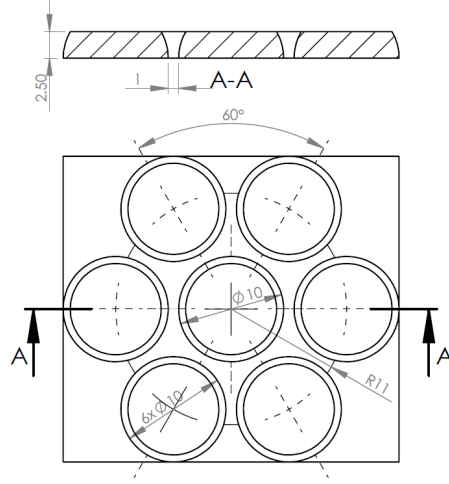
Figure 14: Schematic top view of a unit group of bumps (dimensions expressed in μm).

configuration obtained is represented in Figure 15, from which one can calculate the overall dimension of such bumpy plate:

$$X = 2\left(8x_0 + r_{bump}\right) = 98\,\mu m \tag{4.1}$$

$$Y = 2\left(4\,y_0 + r_{bump}\right) = 86.21\,\mu m \tag{4.2}$$

where x_0 and y_0 are the translation units on axes x and y, respectively. Using trigonometry, they can be found as follows:

$$x_0 = r_{bump} + \frac{d_{b-b}}{2} = 5.5\,\mu m \tag{4.3}$$

$$y_0 = 2\,x_0\,sin(60°) = \sqrt{3}\,x_0 \approx 9.53\,\mu m \tag{4.4}$$

Such quantities will be useful in section 4.1.1, where the 77 bumps will be defined as constraints.

4.1.1 Definition of the constraints

In order to simplify the design of the elytron-textured plate, the reference frame was centered in the central bump, as shown in Figure 15, with axis z orthogonal to the model. In this manner, gravitational energy computation was easier, as explained in 3.4.5. The wet wall was described by three types of constraints: firstly, $z = 0$ was set as the *base plane*, containing all bumps' bases. Secondly, $z = height$ was defined as the *top plane*, the highest flat part of the bump. The macro *height* was defined as half the bump's radius, namely $height = 2.5\,\mu m$. Lastly, the 77 bumps were represented by the equations of just as many spheres, whose centers were translated on the base plane through the units defined in 4.1.

Particularly, each sphere was defined by the following expression:

$$\sqrt{(x - i\,x_0)^2 + (y - j\,y_0)^2 + z^2} = r_{bump} \tag{4.5}$$

where i and j are the multiples of the coordinates $(i\,x_0, j\,y_0)$ of the center of each sphere. Moreover, since it was necessary to name every sphere, each of them was called by the spelled number n referred to its position on the plate, according to the convention defined in Equation 4.6 and Figure 17:

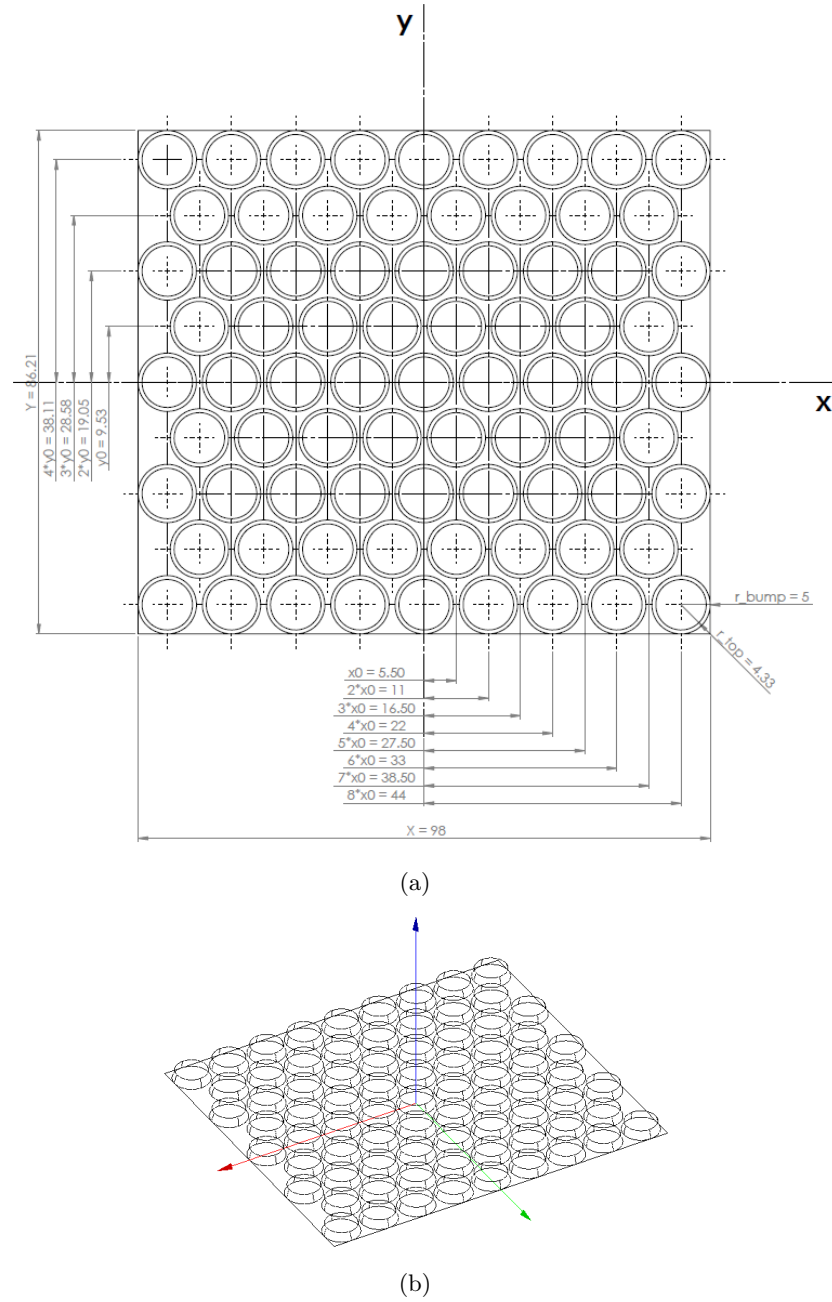$$n = \frac{1}{2}\,i + \frac{17}{2}\,j \tag{4.6}$$

(a)

(b)

Figure 15: (a) Top view of the modelled elytron, showing the hexagonal pattern with detail of the used units x_0 and y_0; (b) SE-FIT's graphic window rendering the bumpy plate (isometric view).

For instance, the bump with coordinates $(5x_0, 3y_0)$ is identified by number $n = \frac{1}{2} \cdot 5 + \frac{17}{2} \cdot 3 = 28$ (therefore, it will be called *twentyeight*) and defined by the following code lines:

```
// Bump (5,3)

constraint twentyeight

formula: sqrt((x−5*x0)^2+(y−3*y0)^2+z^2) = r_bump
```

Finally, the vertices and the sides of each bump, called *edges*, needed to be defined. Each bump is characterized by eight vertices: four for the lower circumference, and four for the upper one. They are linked by twelve edges: four defining the lower circumference, four identifying the upper one, and other four for the side of the sphere. An example can be seen in Figure 16, where the central bump $(0,0)$ is shown: its vertices, indicated by their black numbers, are linked by its edges, highlighted through red identifiers. Such construction was repeated for all 77 bumps, calculating the vertices as a function of the sphere's center and the angular coordinate with respect to it.

Once having defined the wet wall's geometry, in order to perform a simulation, the user must define the vertices, edges, faces and the body of the droplet, in its initial configurations. Then, the integrals to calculate the contribution of the wet wall to the drop's volume, wetted surface and gravitational energy need to be set, focusing in particular on the edges' constraints.

4.2   Centered droplet lying over seven bumps

The first simulation describes the interaction of a water droplet deposited and spreading over seven bumps, whose starting volume is represented by a hexagonal base prism. Such prism is centered on the central bump, with coordinates $(0,0)$ (see Figure 17) and its base lies on the
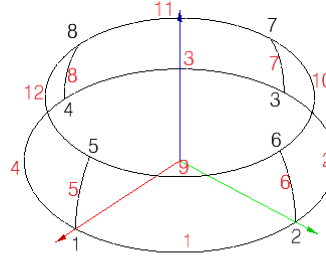
Figure 16: A bump rendered by SE-FIT: the black numbers indicate the vertices, whereas the red ones identify the sides (*edges*). The fixed faces do not change during the convergence, and can be omitted by adding the attribute *bare* to the edges.
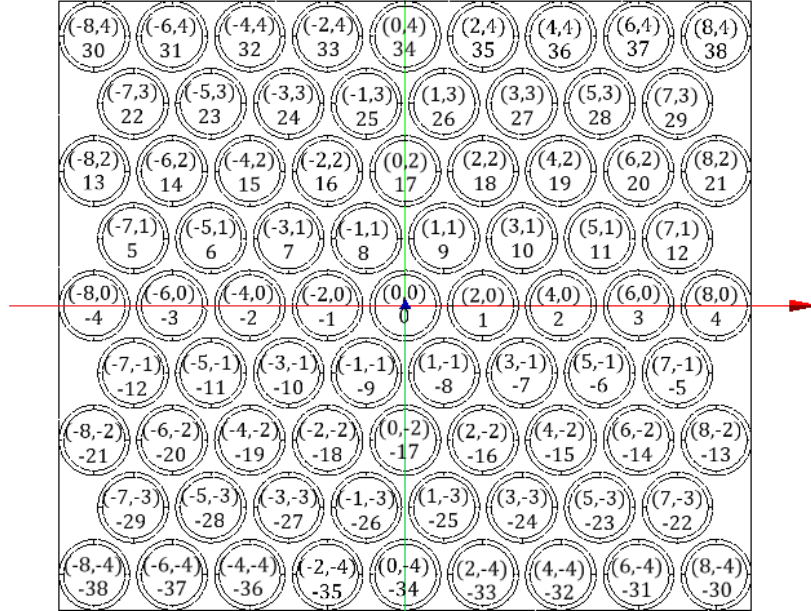
Figure 17: Numbering scheme: each bump is associated with its coordinates (i, j) and is given a number $n = \frac{1}{2} i + \frac{17}{2} j$.
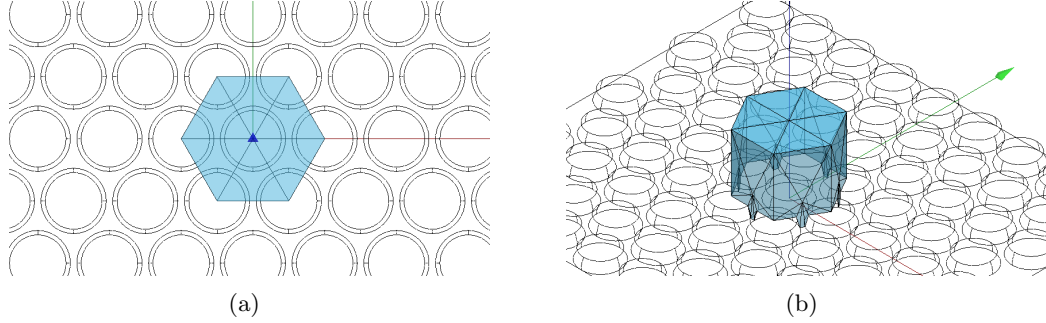
Figure 18: Initial configuration of the water droplet: (a) top view of hexagonal prism with base's edges following the bumpy profile; (b) isometric view showing the prism supported by the first ring of bumps.

six surrounding bumps. It is helpful to refer to these six bumps as the *first ring* of bumps, to distinguish them from the *second ring*, surrounding the previous one.

With the aim of assuring the contact between the liquid droplet and the wet wall, the contact line was defined following the wall's morphology, specifically modifying the prism's edges at its base, as can be seen in Figure 18a. Particularly, each side of the hexagon was split into five smaller edges, so that each one could be constrained to the belonging feature (top plane, side of a bump, or base plane). Such constraints impose a condition for the reliability of the simulation, which is valid as far as the contact line keeps itself on the initially defined constraint. Since the contact line advances or recedes as a function of the liquid volume, this condition leads to a range of volumes for which the simulation is valid. For instance, iteratively running the script with volumetric variation, one can find that the present simulation is valid for droplets between $0.75\,pL$ and $3.00\,pL$.

4.2.1   Calculation of the body integrands

As found in section 3.4.5, the wet wall contribution to the integrals for volume, wetted surface area and gravitational energy depends on the value of the vector fields crossing the liquid/solid interface. Recalling Equation 3.45, Equation 3.51 and Equation 3.60, such vector fields can be obtained from the constraint geometry $z = f(x, y)$,:

- Volume contribution of the wet wall, v_{stuff}:

$$v_{stuff}(x, y) = \int f(x, y)\, dx \qquad (4.7)$$

- Wet wall surface area, w_{ye}:

$$w_{ye}(x, y) = \int \sqrt{1 + \left(\frac{\partial f}{\partial x}\right)^2 + \left(\frac{\partial f}{\partial y}\right)^2}\, dx \qquad (4.8)$$

- Gravitational energy contribution of the wet wall, g_{stuff_z}:

$$g_{stuff_z}(x, y) = \int \frac{1}{2} f^2(x, y)\, dx \qquad (4.9)$$

In the present case, it is possible to see that the vector field $z = f(x, y)$ is not continuous on the integration domain: particularly, it is null on the base plane, A_0, it varies according to the profile of the spherical bumps on $A_{\tilde{z}}$ and finally reaches the value $z = height = 2.5\,\mu m$ on the top plane, A_{height}. In Figure 19, the three subdomain are graphically distinguished by color. Thanks to the integral' additivity property, the integration on the whole domain can be split
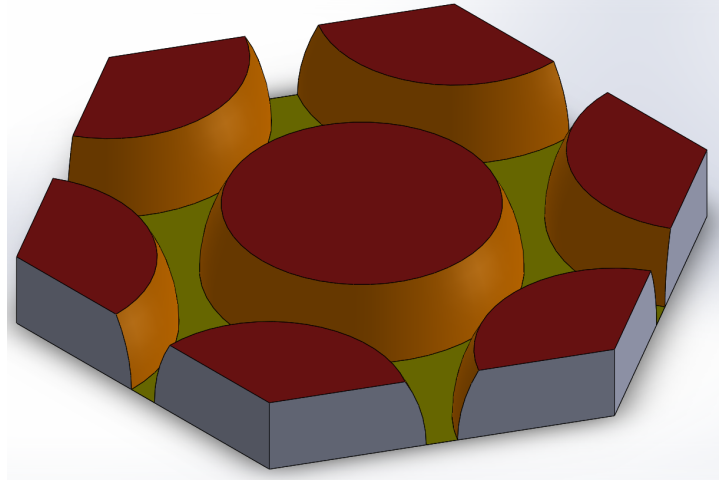
Figure 19: Solid/liquid interface at the initial configuration, with different colors indicating different value of $z = f(x, y)$: yellow for A_0, orange for $A_{\bar{z}}$ and red for A_{height}

into a sum of three integrals, executed on the smaller areas wherein the function $z = f(x, y)$ is continuous. However, since the inner borders of the subdomains are not part of the contact line and thus are not defined in the script, it is not possible to impose suitable constraints on them.

Alternatively, the integrals' linearity allows to apply the mean value theorem on the integration domain: the goal is to find a mean constant value $\bar{z}$ for $z = f(x, y)$ over the whole integration domain (i.e. the wet wall), such that, multiplying it by the liquid/solid interface area, one obtains the value of the investigated integral. Recalling Equation 3.41 for the volume contribution from the wet wall, V_{ls}, $\bar{z}$ is now sought, as follows:

$$V_{ls} = \int_{\partial B_{ls}} z\vec{k} \cdot \vec{n} \, dA = \bar{z} \cdot \partial B_{ls} \tag{4.10}$$
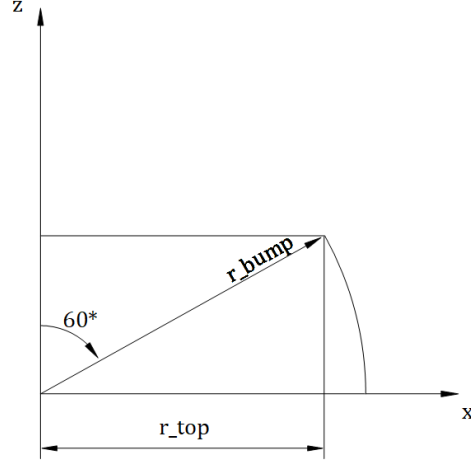
Figure 20: Reference for the calculation of the average value of z over the bump's side, $\tilde{z}$.

Hence, the searched value $\bar{z}$ is the average value of $z = f(x, y)$ over the integration domain, weighted with respect to the subdomains. It can be calculated by considering the three subdomains one at a time:

- $z = height = 2.5\,\mu m$ over A_{height}: A_{height} corresponds to the red surface in Figure 19, given by the central bump top and by six $\frac{2\pi}{3}$ circular sectors. Hence,

$$A_{height} = \pi\, r_{top}^2 + 6 \cdot \frac{2\pi}{3}\, \frac{r_{top}^2}{2} = 3\pi\, r_{top}^2 \tag{4.11}$$

- $z = \tilde{z}$ over $A_{\tilde{z}}$: $A_{\tilde{z}}$ sums up the side of the central bump and the interested parts of the six surrounding bumps' sides. On such subdomain, z can be averaged on the bump's side, obtaining a value $\tilde{z}$. With reference to Figure 20, one has:

$$\tilde{z} = \frac{1}{r_{bump} - r_{top}} \int_{r_{top}}^{r_{bump}} \sqrt{r_{bump}^2 - x^2} \, dx \approx 1.69 \, \mu m \tag{4.12}$$

$$A_{\tilde{z}} = \int_{0}^{2\pi} \int_{\frac{\pi}{3}}^{\frac{\pi}{2}} r_{bump}^2 \, sin\phi \, d\phi d\theta + 6 \cdot \int_{0}^{\frac{2\pi}{3}} \int_{\frac{\pi}{3}}^{\frac{\pi}{2}} r_{bump}^2 \, sin\phi \, d\phi d\theta = 3\pi r_{bump}^2 \tag{4.13}$$

- $z = 0$ over A_0: A_0 results from the area of the hexagon except for the projection of the bumps on the $x - y$ plane.

$$A_0 = A_{hex} - \pi r_{bump}^2 - 6 \cdot \frac{2\pi}{3} \frac{r_{bump}^2}{2} = 6\sqrt{3} \, x_0^2 - 3\pi r_{bump}^2 \tag{4.14}$$

Thus, one can finally calculate:

$$\bar{z} = \frac{A_{\tilde{z}}\tilde{z} + A_{height}height}{A_0 + A_{\tilde{z}} + A_{height}} = \frac{3\pi r_{bump}^2 \tilde{z} + 3\pi r_{top}^2 height}{6\sqrt{3} \, x_0^2 + 3\pi r_{top}^2} \approx 0.69088 \, \mu m \tag{4.15}$$

By substituting the result of Equation 4.15 into Equation 4.7, Equation 4.8 and Equation 4.9, and solving the ODE, it was possible to obtain the body integrands, which were assigned to
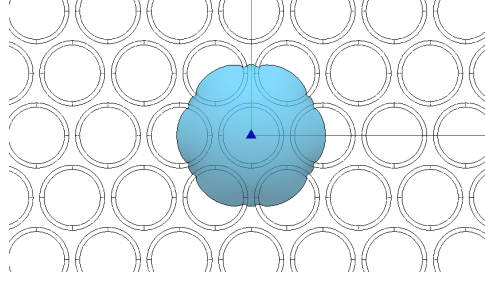
Figure 21: $2.0\,pL$ droplet in equilibrium condition, spread on 7 bumps (bump diameter $10\,\mu m$).

the edges constraints, namely the six bumps of the first ring, the base plane and the top plane.

Particularly, one has:

$$
\begin{cases}
v_{stuff} = \bar{z}\,x \\[2ex]
w_{ye} = cos\theta\,x \\[2ex]
g_{stuff_z} = \frac{1}{2}\bar{z}^{\,2}\,x
\end{cases}
\tag{4.16}
$$

In summary, to set a simulation, the geometry of the droplet, its constraints and the body inte-grands for the computation of the wet wall are required. Once having obtained all the necessary quantities, the iterative convergence can be started, leading to the equilibrium configuration represented in Figure 21.

4.3   Centered droplet lying over nineteen bumps

As explained in section 4.2, the first simulation can reliably predict the equilibrium shape for droplet volume between $0.75\,pL$ and $3.00\,pL$, corresponding to characteristic lengths between $5.5\,\mu m$ and $9.0\,\mu m$, calculated through Equation 3.22. Hence, in order to study larger droplets
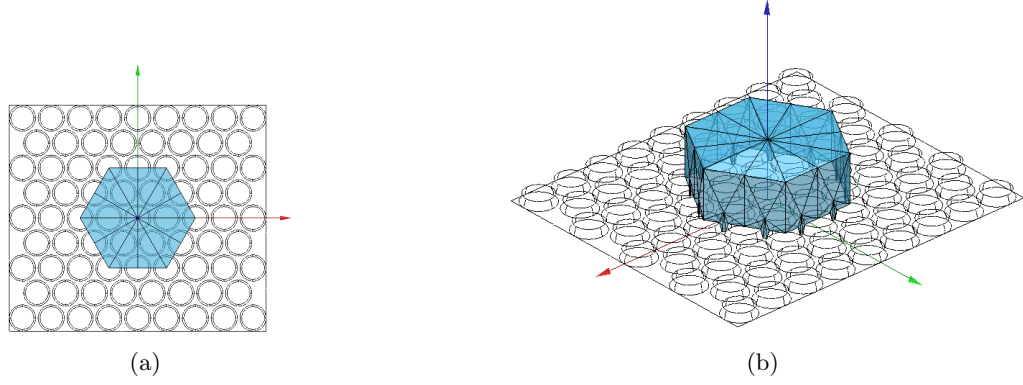
Figure 22: Initial configuration of the water droplet: (a) hexagonal prism with base's edges following the bumpy profile; (b) top view showing the prism supported by the second ring of bumps.

interacting on the studied micro-textured surface, in was chosen to enlarge the contact line, shifting it to the second ring of bumps. The starting hexagonal base prism configuration was maintained, as shown in Figure 22. The initial boundary conditions for the contact line are the same as in the previous case, except that the base sides are now split into nine edges, to fit three bumps instead of two.

The simulation can be structured as in section 4.2, defining the droplet's initial geometry and evaluating the body integrands as a function of the new liquid/solid interface.
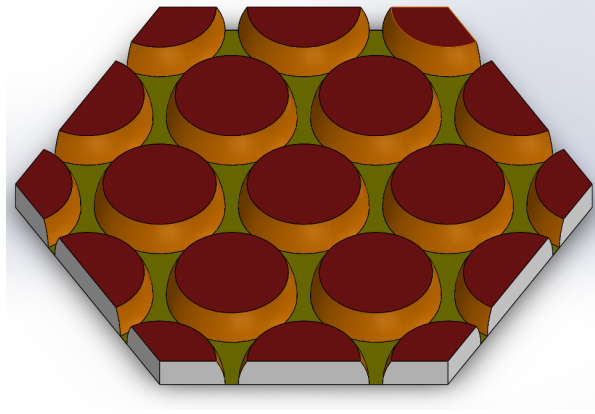
Figure 23: Solid/liquid interface at the initial configuration, with different colors indicating different value of $z = f(x, y)$: yellow for A_0, orange for $A_{\tilde{z}}$ and red for A_{height}

4.3.1   Calculation of the body integrands

Analogously to the procedure in 4.2.1, the solid/liquid interface is divided into subdomains, on which the function $z = f(x, y)$, or its average on the subdomain, is known. Its values do not change with respect to the previous simulation, thus:

$$
\begin{cases}
z = 0 & on \quad A_0 \\[2ex]
z = \tilde{z} \approx 1.69 \, \mu m & on \quad A_{\tilde{z}} \\[2ex]
z = height = 2.5 \, \mu m & on \quad A_{height}
\end{cases}
\tag{4.17}
$$

The liquid/solid interface appears similar to the previous case. Thus, the required quantities were computed, with reference to terrain shown in Figure 23.

- A_{height}, red surface: the summit of the central bump, of the first ring of bumps and of the twelve in the second ring. Such area can be calculated as:

$$A_{height} = 7\pi \, r_{top}^2 + 6 \, \frac{\pi}{2} \, r_{top}^2 + 6 \, \frac{\pi}{4} \, r_{top}^2 = 12\pi \, r_{top}^2 \qquad (4.18)$$

- $A_{\tilde{z}}$, orange surface: the sides of the nineteen bumps wetted by the droplet. Hence:

$$
\begin{aligned}
A_{\tilde{z}} = &\, 7 \int_0^{2\pi} \int_{\frac{\pi}{3}}^{\frac{\pi}{2}} r_{bump}^2 \, sin\phi \, d\phi d\theta + 6 \int_0^{pi} \int_{\frac{\pi}{3}}^{\frac{\pi}{2}} r_{bump}^2 \, sin\phi \, d\phi d\theta + \\
&+ 6 \int_0^{\frac{2\pi}{3}} \int_{\frac{\pi}{3}}^{\frac{\pi}{2}} r_{bump}^2 \, sin\phi \, d\phi d\theta \\
&= 7\pi \, r_{bump}^2 + 6 \, \frac{\pi}{2} \, r_{bump}^2 + 6 \, \frac{\pi}{3} \, r_{bump}^2 = 12\pi \, r_{bump}^2
\end{aligned}
\qquad (4.19)
$$

- A_0, yellow surface, computable as the difference between the hexagonal base and the projections of the bumps on the $x - y$ plane:

$$A_0 = A_{hex} - 7\pi \, r_{bump}^2 - 6 \, \frac{\pi}{2} r_{bump}^2 - 6 \, \frac{\pi}{3} r_{bump}^2 = 6 \, 4\sqrt{3} \, x_0^2 - 12\pi r_{bump}^2 \qquad (4.20)$$

Hence, grouping together Equation 4.18, Equation 4.19, and Equation 4.20, one can calculate the average value of $z = f(x, y)$ over the integration domain:

$$\bar{z} = \frac{A_{\tilde{z}} \, \tilde{z} + A_{height} \, height}{A_0 + A_{\tilde{z}} + A_{height}} = \frac{12\pi r_{top}^2 \, height + 12\pi r_{bump}^2 \, \tilde{z}}{6 \cdot 4\sqrt{3} \, x_0^2 + 12\pi r_{top}^2} \approx 0.58573 \, \mu m \qquad (4.21)$$
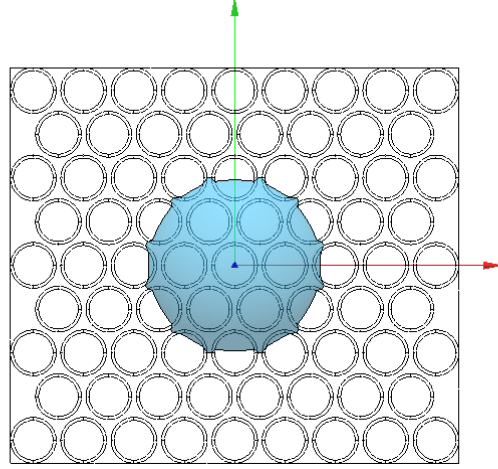
Figure 24: $8.0\,pL$ droplet in equilibrium condition, spread on 19 bumps (bumps' diameter $10\,\mu m$).

By substituting such quantity in the ODEs for the integrands' computation, the same result as Equation 4.16 is achieved. Finally, the simulation is ready to be run to the equilibrium condition, shown in Figure 24. Iteratively running the simulations by varying the volumetric parameter, it is possible to identify the volume range guaranteeing its validity, namely for droplets between $8.0\,pL$ and $15.0\,pL$.

4.4   Results and discussion

A $2.0\,pL$ volume water droplet spreading on seven bumps was considered. From SE-FIT's graphic window, isometric, planar and cross-section views are obtained, as shown in Figure 25. SE-FIT's outcome refers to the water/air interface, colored in light blue in the figure: the volume in between the wet wall and the highlighted surface is filled with water. As expected, being centered on the central bump $(0,0)$, the droplet presents a nearly axisymmetric shape.

Globally, the droplet is lying on the bumps, with the water steeply penetrating in the grooves (Figure 25d). The $22.8\,\mu m$ spreading distance can be evaluated from side to side as shown in Figure 26, where the measurement was executed on the top of the bumps.

As predicted by Wenzel's model [9], the contact angle on the top of the bumps decreases, due to surface roughness, which always accentuates the wettability of materials [10]: particularly, the contact angle on top of the bump measures $59.4°$, as measured from a planar section through the middle of the hexagonal configuration (Figure 25c). By contrast, the opposite was observed in the grooves, which lead to an an increase in contact angle up to approximately $87°$, at the bottom of the valley (Figure 25d).

Lastly, SE-FIT allows the user to know the *Total Area* of the droplet exposed to air, namely the air/water interface, which for the present volume measures $524.1\,\mu m^2$.

4.4.1   Application of Wenzel's model to the simulation

In order to calculate a global averaged value for the contact angle, the lengths of the contact line between the bumps were measured through *Autodesk AutoCAD*'s *Measure Distance* function as $1.30\,\mu m$. Similarly, the contact line's perimeter was evaluated as $71.1\,\mu m$. Thus, the contact angles measured in the different sections were averaged, weighted with respect to the contact line:

$$\theta^*_{SE-FIT} = \frac{6 \cdot 1.30\,\mu m\,87° + (71.1\,\mu m - 6 \cdot 1.30\,\mu m)\,59.4°}{71.1\,\mu m} = 62.4° \qquad (4.22)$$
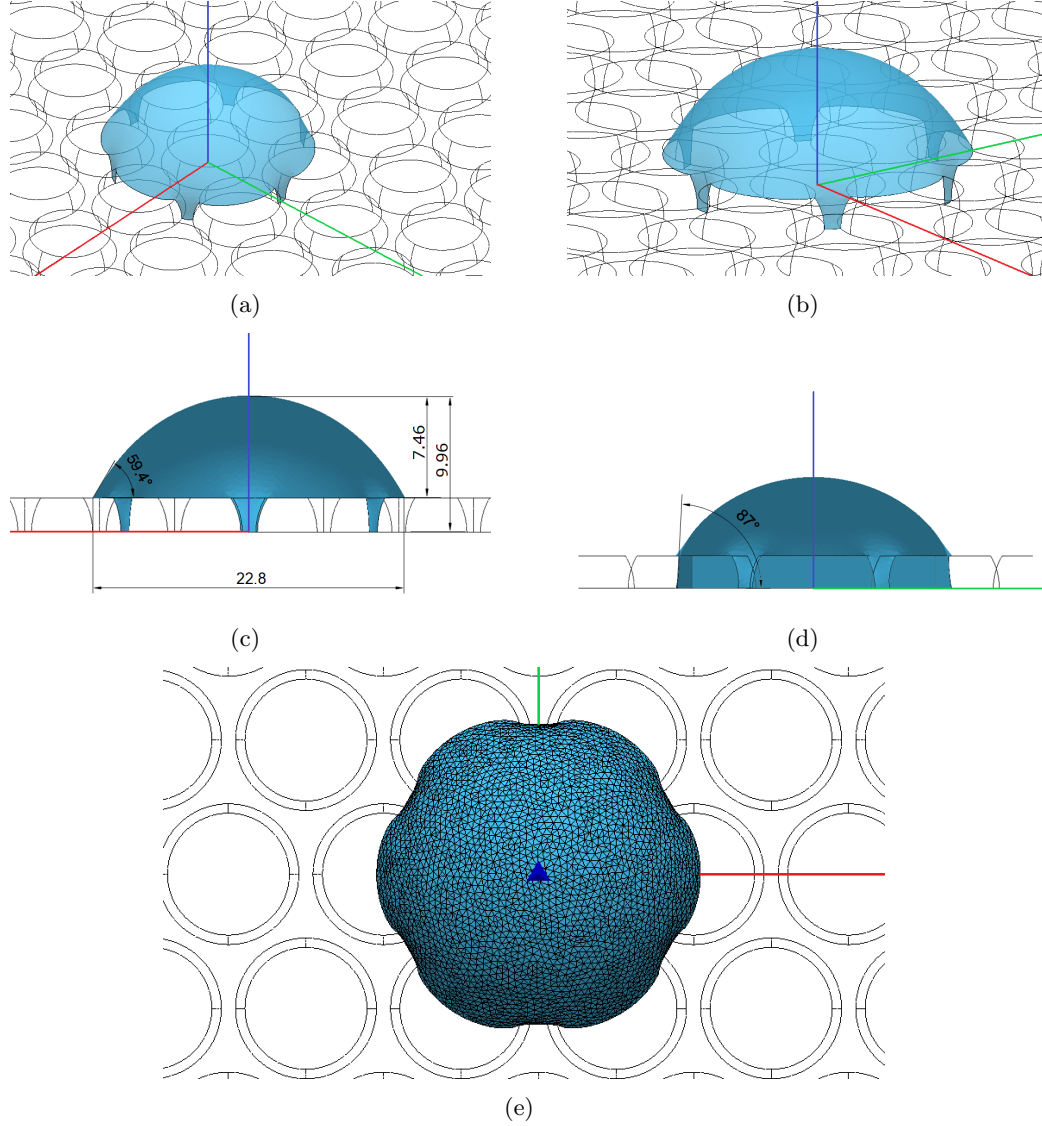
Figure 25: Graphic rendering of a $2.0\,pL$ droplet lying over 7 bumps (axes x, y, and z shown in red, green and blue, respectively): (a) Overall isometric view; (b) Detail of the water *pillars* between the bumps; (c) Cross section through $x - z$ plane, showing the maximum spreading distance and the equilibrium contact angle with the top of the bump; (d) Cross section through $y - z$ plane, showing the minimum spreading distance and the equilibrium contact angle with the valley; (e) Top view of the droplet, detailing mesh refinement and irregular contact line due to the wet wall's bumpiness.

Therefore, following Wenzel's model, one can define the surface roughness as the ratio between the actual liquid/solid interface area A_{act} and the apparent one A_{app}, namely the droplet's projection on the $x - y$ plane, measuring $386.7\,\mu m^2$ (from *Autodesk AutoCAD*'s *Measure Area* function applied on Figure 26). The actual area was instead evaluated from A_{app} as explained in Equation 4.23:

$$A_{act} = A_{app} - \pi(r_{bump}^2 - r_{top}^2) - 6 \cdot \frac{\beta}{2}(r_{bump}^2 - r_{top}^2) + \pi r_{bump}^2 + 6 \cdot \frac{\beta}{2}r_{bump}^2 = 590.5\,\mu m^2 \quad (4.23)$$

With reference to the middle section of Equation 4.23, the second and third term are the projections of the covered portions of bumps' sides on the $x - y$ plane, to subtract from A_{app} in order to obtain the flat portion of the actual area. The angle $\beta = 147°$ identifies the covered portion of the bump, as shown in Figure 26; the fourth and the fifth terms refer to the area of the bump sides, in contact with water.

Thus, with such values one can write:

$$r = \frac{A_{act}}{A_{app}} = 1.53 \quad (4.24)$$

Hence, through Wenzel's relation, the predicted contact angle is calculated from the equilibrium contact angle of the material, $\theta_E = 70°$, as follows:

$$\theta_{Wenzel}^* = arccos(r\,cos\theta_E) = 58.5° \quad (4.25)$$
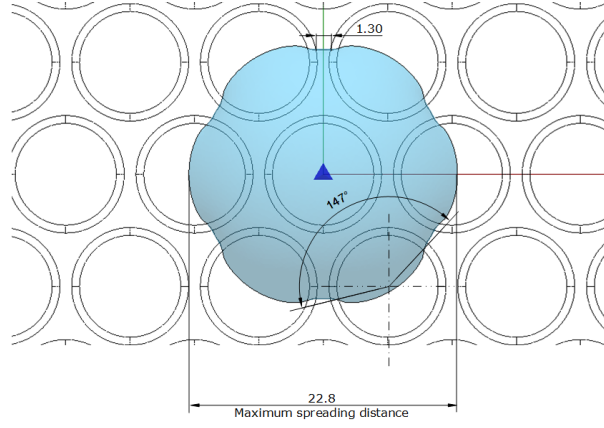
Figure 26: Top view of the droplet, omitting the mesh (dimensions in μm).

Finally, one can compare such result with the averaged contact angle, calculated in Equation 4.22, evaluating the relative error:

$$error = \frac{\theta^*_{SE-FIT} - \theta^*_{Wenzel}}{\theta^*_{Wenzel}} = 6.76\% \qquad (4.26)$$

In conclusion, the difference between the measured value and that deriving from physic model is acceptable, which leads to the validity of Wenzel's model in the current physical configuration.

4.4.2 Assessment of the *total area* parameter calculation

A good way to validate the SE-FIT simulation is comparison with analytical measurement of lateral surface area for equilibrium shape of droplet on a flat surface. For example, from literature [9], it is known that the equilibrium condition for a droplet on a flat plane in partial wetting regime is given by a spherical cap, resting on the substrate with a contact angle θ_E.

Then, it is sufficient to analytically calculate the area of a spherical cap, intersected by an horizontal plane forming an angle θ_E with the tangent to the sphere. Then, comparing the results from geometry and the program's outcome in a flat surface case, the computational error made by SE-FIT can be evaluated.

The analytical calculation starts from the liquid volume, constituting the volume of the spherical cap. From geometry [17], it is known that considering a sphere with radius R, the volume of a spherical cap of height h and base radius a is given by the following equation:

$$V_{cap} = \frac{1}{6}\pi h(3a^2 + h^2) \tag{4.27}$$

With reference to Figure 27, the following relations are derived:

$$a = Rsin\theta \tag{4.28}$$

$$h = R - Rcos\theta = R\left(1 - cos\theta\right) \tag{4.29}$$

Substituting Equation 4.28 and Equation 4.29 into Equation 4.27, one obtains the following expression:

$$V_{cap} = \frac{1}{3}\pi R^3 \left(2 - 3cos\theta + cos^3\theta\right) \tag{4.30}$$

From which is possible to find the radius of the sphere, R:

$$R = \sqrt[3]{\frac{3V_{cap}}{\pi(2 - 3cos\theta + cos^3\theta)}} \tag{4.31}$$
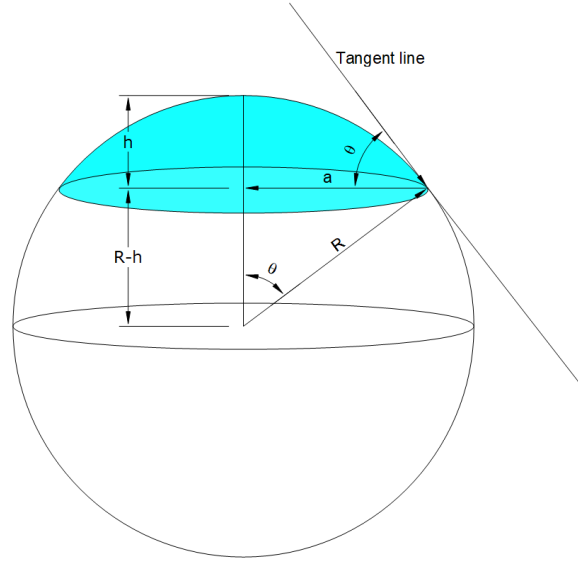
Figure 27: Geometric scheme for a spherical cap's area calculation.

Hence, knowing the radius from Equation 4.31, the height of the cap, h, from Equation 4.29, one can compute the spherical cap's area, namely:

$$A_{cap} = 2\pi Rh \qquad (4.32)$$

Equation 4.32 was used to calculate the spherical caps produced by different volume droplets. Then, a new simulation was performed in SE-FIT, defining the wet wall as an ideal flat surface:

it was then run iteratively varying the volume of the droplet. Hence, the percentage relative error between the cap's area from geometry and the one from SE-FIT was calculated as follows:

$$error = \frac{A_{cap}^{SE-FIT} - A_{cap}}{A_{cap}} \qquad (4.33)$$

Such percentage error is reported for each droplet's volume in the scatter plot in Figure 28. The error, in absolute value, never exceeds 0.06%, thus being certainly negligible. Therefore, it is possible to state that SE-FIT's *Total Area* evaluation is reliable.
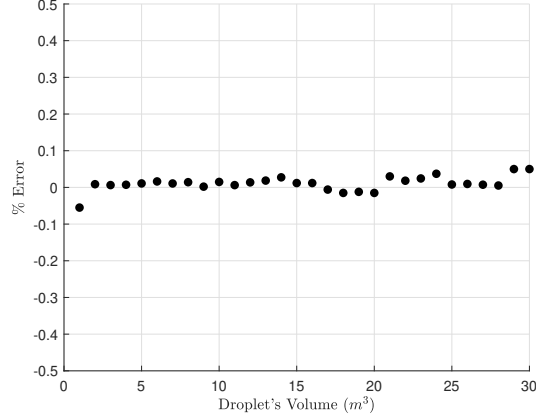

Figure 28: SE-FIT's percentage error in air/water interface evaluation for different droplet volumes.
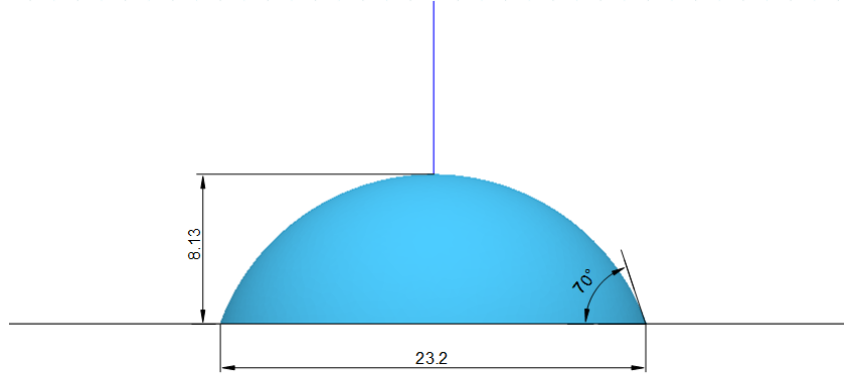
Figure 29: Side view of a SE-FIT simulated water droplet lying on a smooth flat surface, assuming a spherical cap shape and showing an equilibrium contact angle θ_E. Dimensions in μm.

4.4.3   Micro-texture aiding in reduction of droplet lateral surface area

The droplet area exposed to air plays an important role in the droplet's evaporation: larger air/water interfaces correspond to higher evaporation rate, since the number of surface molecules able to escape per unit volume is higher. It is useful to the present analysis to compare the total area exposed to air of an equilibrium-configuration droplet on a textured surface versus a flat surface. For a $2\,pL$ droplet volume, the lateral surface area computed using SE-FIT for a droplet spreading on a flat surface is $630.6\,\mu m^2$, which is comparable to the analytically calculated value.

However, the total area exposed to air is $524.1\,\mu m^2$ for the droplet on the textured surface: it is clear that the air/water interface is lower when the droplet is in contact with the bumpy

surface than on the smooth one. Particularly, bump induced roughness decreases the total area

by:

$$\Delta A_\% = \frac{A_{flat} - A_{bumpy}}{A_{flat}} = 16.9\% \tag{4.34}$$

In addition, as can be seen from Figure 26 and Figure 29, the spreading distance does not look

to change very much in the two cases, varying from $22.8\,\mu m$ on the bumpy surface to $23.2\,\mu m$

on the flat one. The shapes of the considered droplets are comparable, which may be explained

considering that, on the micro-textured surface, part of the droplet's volume can fill the voids

between the bumps, "hiding" from the outside air. The air/water interface reduction may

have consequences on water evaporation on the bumpy micro-textured surface, which might be

observed slower than on an ordinary flat wall.

In order to better understand the observed phenomenon, larger droplets needed to be an-

alyzed. For this purpose, the second simulation was used, considering an $8.0\,pL$ droplet lying

over nineteen bumps. The graphic outcome from SE-FIT can be seen in Figure 30.

Similarly to the previous simulation, the characteristics of the droplet are evaluated:

  - Spreading distance : $37.4\,\mu m$;

  - Contact angle at the top of the bump: $60.1°$;

  - Total Area: $1486.6\,\mu m$.

In agreement with what observed above, the contact angle is lower than the material's equilib-

rium contact angle. From the comparison with a $8.0\,pL$ water droplet wetting a flat surface,

shown in Figure 31, it is noticeable that both the spreading distance and the droplet's height
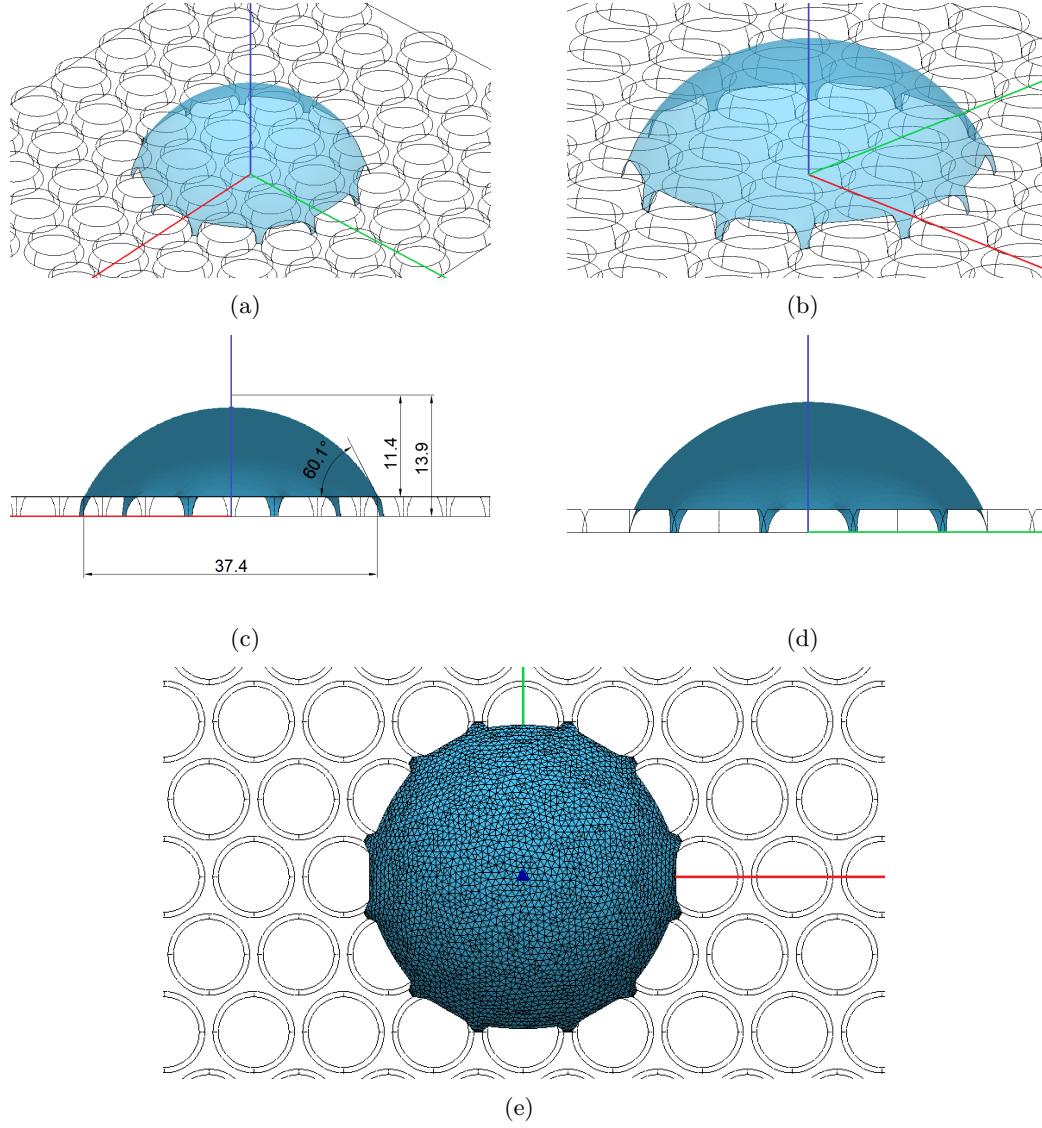
Figure 30: Graphic rendering of a $8.0\,pL$ droplet lying over 19 bumps (axes x, y, and z shown in red green and blue, respectively): (a) Overall isometric view; (b) Detail of the water *pillars* between the bumps; (c) Cross section through $x - z$ plane, showing the spreading distance, the equilibrium contact angle at the top of the bump and the height of the droplet with respect to top and base planes; (d) Cross section through $y - z$ plane; (e) Top view of the droplet, detailing mesh refinement and irregular contact line due to the wet wall's roughness.
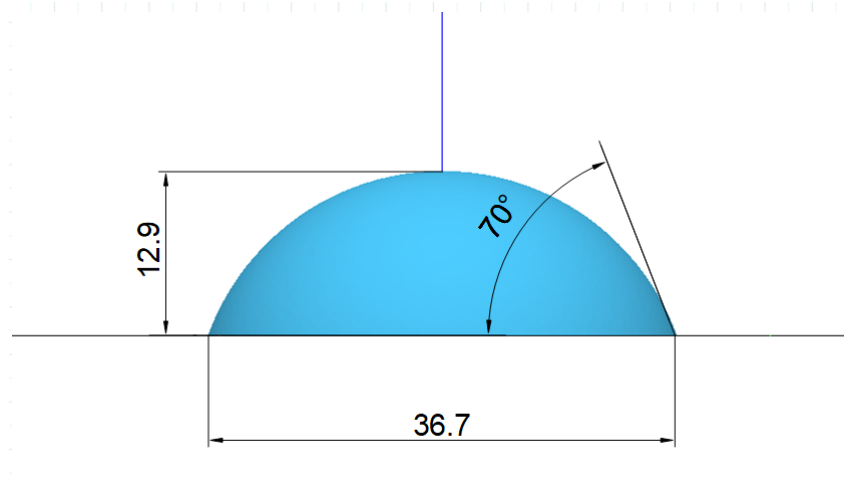
Figure 31: $8.0\,pL$ water droplet wetting flat surface profile shape. Dimensions in μm.

undergo very little variation, confirming what observed in the previous simulation.

The air/water interface in the flat wall case measures $1589.1\,\mu m$, whereas it reduces to $1486.6\,\mu m$ when the droplet lies on the micro-textured surface. Thus, it is possible to calculate the percentage reduction, as follows:

$$\Delta A_\% = \frac{A_{flat} - A_{bumpy}}{A_{flat}} = 6.45\% \tag{4.35}$$

In conclusion, the second simulation, executed on a larger droplet with volume $8.0\,pL$, produced the same kind of result as the previous one, strengthening the hypothesis that the such bump related roughness causes a reduction of the air/water interface, thus decreasing the evaporation of the droplet.

4.4.3.1   Effect of bump-to-bump distance reduction

The analysis performed so far always used a micro-textured surface presenting a hexagonally-patterned distribution of bumps separated from one another by $1\,\mu m$ at the base. However, as can be seen in the ESEM micrographs (Figure 13), on the beetle's elytron the space between the elevations is very narrow. Although separating the bumps was necessary to avoid singularities in the simulations, it is fundamental to understand what happens by decreasing the *bump-to-bump distance d_{b-b}*, as far as such singularities do not appear, in order to further examine the air/water interface reduction phenomenon.

Therefore, two series of simulations were executed, with a droplet lying on seven bumps and with one wetting nineteen elevations, respectively: for each series, the liquid volume was kept constant, as well as the bump's radius. Particularly, the latter was set at $5\,\mu m$, as observed on the beetle elytra. Hence, for each run, the bump-to-bump distance was varied, and the percentage air/water interface area reduction was evaluated through the following:

$$\Delta A_\% = \frac{A_{flat} - A_{bumpy}}{A_{flat}} \tag{4.36}$$

As shown in Table I, for the simulation of the droplet lying on seven bumps the volume was set at $2.0\,pL$, whereas in the second simulation, a $8.0\,pL$ droplet wets nineteen bumps, as reported in Table II. Running such simulations, it was possible to obtain the curves shown in Figure 32 and Figure 33.

Both the curves show that the closer are the bumps, the more accentuated is the interface

area reduction phenomenon, although the increase of the relative reduction is limited to some percentage point. Particularly, for the smaller $2.0\,pL$ droplet, a further 1.26% reduction is achieved by reducing the bump-to-bump distance from $3\,\mu m$ to $1\,\mu m$. On the other hand, the percentage reduction benefits of a further 3.24% less by decreasing the grooves' width from $1\,\mu m$ to $0.1\,\mu m$. Besides this, it is also noticeable that the simulation with nineteen bumps is less affected by singularities, since the contact line spreads more and enlarges by moving away from the axis z. Further simulation series were executed for other droplet volumes, returning the same result: the relative graphs are here omitted in order to avoid redundancy.

In summary, for all the considered volumes the percentage Total Area reduction shows the same decreasing trend with decreasing bump-to-bump distance. Therefore, such phenomenon looks to be independent of the droplet's volume itself. Consequently, further analyses will not be affected by the choice of the bump-to-bump distance, which will be fixed to make other parameters variable.

4.4.3.2   Effect of bump radius variation

In section 4.4.3.1 it was demonstrated that the air/water interface area variation can be studied independently of the distance between the bumps, d_{b-b}. As will be observed soon, such result will be helpful in the following analysis. Specifically, it is now interesting to investigate how the bumps' radius r_{bump} affects the total area reduction, looking for some *optimal* condition to minimize water evaporation on the micro-textured surface.

For this purpose, similarly to the procedure in section 4.4.3.1, new series of simulations were run, this time keeping d_{b-b} constant and varying the feature radius. Figure 35 summarizes the

Figure 32: Percentage variation of the air/water interface $\Delta A_\%$ as a function of the distance between the bumps d_{b-b} for a $2.0\,pL$ droplet.

TABLE I: BUMP-TO-BUMP DISTANCE AND PERCENTAGE AIR/WATER INTERFACE REDUCTION FOR A $2.0\,pL$ WATER DROPLET LYING ON SEVEN BUMPS

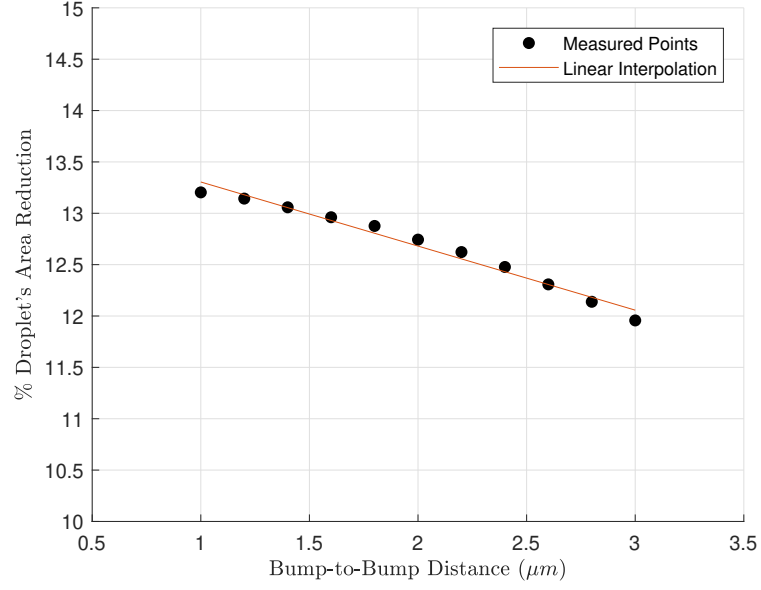| $d_{b-b}\,(\mu m)$	$\Delta A_\%$
1.0	13.20%
1.2	13.14%
1.4	13.06%
1.6	12.96%
1.8	12.88%
2.0	12.74%
2.2	12.62%
2.4	12.48%
2.6	12.31%
2.8	12.14%
3.0	11.96%
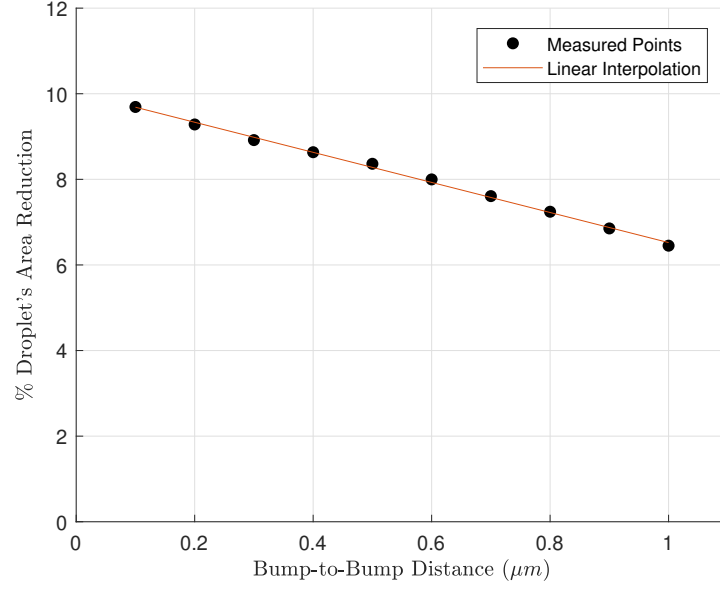
Figure 33: Percentage variation of the air/water interface $\Delta A_\%$ as a function of the distance between the bumps d_{b-b} for a $8.0\,pL$ droplet.

TABLE II: BUMP-TO-BUMP DISTANCE AND PERCENTAGE AIR/WATER INTERFACE REDUCTION FOR AN $8.0\,pL$ WATER DROPLET LYING ON NINETEEN BUMPS

$d_{b-b}\,(\mu m)$	$\Delta A_\%$
0.1	9.69%
0.2	9.28%
0.3	8.92%
0.4	8.63%
0.5	8.36%
0.6	8.00%
0.7	7.61%
0.8	7.24%
0.9	6.85%
1.0	6.45%

results for a $3.0\,pL$ water droplet lying on seven bumps, separated from one another by $1.6\,\mu m$. It is possible to individuate an asymptotic trend towards an optimal condition, after which the area reduction cannot increase anymore. Particularly, for a $3.0\,pL$ droplet such condition determines a maximum air/water interface area reduction around 20%. Looking at the droplet's shape evolution with increasing r_{bump} in Figure 34, it is noticeable that the droplet's height gradually decreases: the liquid looks like tending to a condition when it is completely spread inside the grooves. In such situation, as least liquid as possible is exposed to air, and ideally water would form a film skimming the summit of the bumps. Since the Total Area cannot be reduced further, this state coincides with the maximum air/water interface area reduction. Running simulations on droplets with different volumes will lead to curves with common asymptotic trend, as shown in Figure 36. It is noticeable that the curves do not overlap, but are translated on the $\Delta A_\% - r_{bump}$ plane: this may be explained by the fact that the entire problem depends on the droplet's volume. As a matter of fact, for larger droplets, the optimal air/water interface area reduction is higher, leading to major benefits in terms of limiting evaporation. In order to compare data from different droplet volumes, it is necessary to non-dimensionalize the problem: this can be achieved by relating the bump radius r_{bump} to a proper characteristic length scale, in turn dependent on the droplet volume. The spreading radius of the droplet over a flat surface (Equation 4.28) is suitable to such goal, being dependent of the droplet volume as follows:

$$a = \sqrt{\frac{6V_{cap}}{3\pi h} - \frac{h^2}{3}} \tag{4.37}$$

where h is the height of the spherical cap. Thus, the *non-dimensional bump radius* r^*_{bump} was calculated and associated to the correspondent percentage area reduction evaluated for Figure 36:

$$r^*_{bump} = \frac{r_{bump}}{a} \qquad (4.38)$$

Hence, the obtained data points $(r^*_{bump}, \Delta A_\%)$ were reported on a scatter plot, as shown in Figure 37. As can be seen, this non-dimensionalization led to independence of volume for the curve: the percentage area reduction monotonically increases with the non-dimensional bump radius, until $r^*_{bump} \approx 0.5$, where it reaches a plateau, stabilizing around 20%. Hence, it is possible to define an engineering design criterion irrespective of volume of impacting droplet to design an optimal morphology, able to minimize the evaporation rate of water depositing on such micro-textured surface: given a droplet volume $V_{droplet}$, for which a can be evaluated, the optimal lateral area reduction is achieved for:
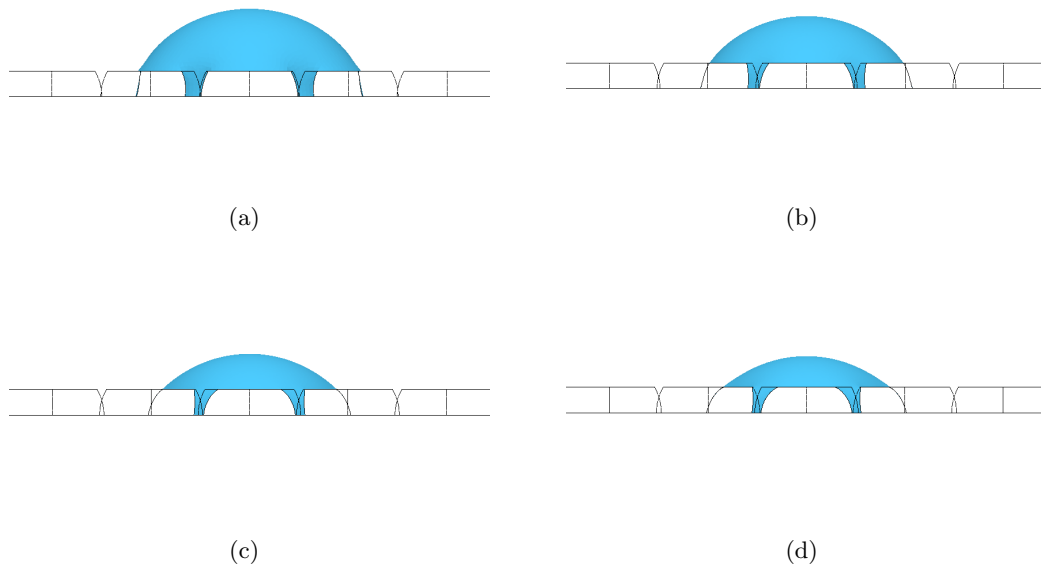
$$r^{opt}_{bump} = 0.5\,a \qquad (4.39)$$

(a)

(b)

(c)

(d)

Figure 34: $3.0\,pL$ droplet's shape evolution with changing bumps' radius: (a) $r_{bump} = 5\,\mu m$; (b) $r_{bump} = 6\,\mu m$; (c) $r_{bump} = 7\,\mu m$; (d) $r_{bump} = 8\,\mu m$

Figure 35: $3.0\,pL$ water droplet: percentage variation of the air/water interface $\Delta A_\%$ as a function of the bumps' radius r_{bump}.

TABLE III: BUMP RADIUS AND PERCENTAGE AIR/WATER INTERFACE REDUCTION FOR A $3.0\,pL$ WATER DROPLET LYING ON SEVEN BUMPS

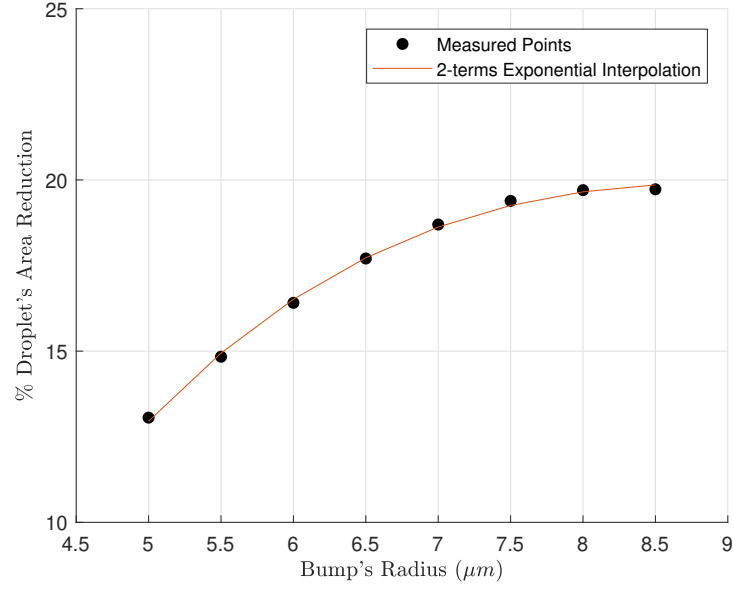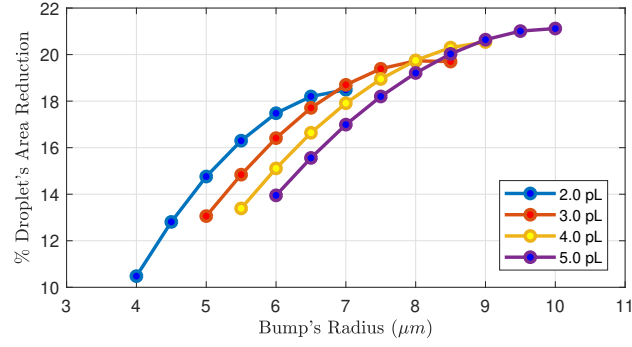| $r_{bump}\,(\mu m)$	$\Delta A_\%$
5.0	13.06%
5.5	14.84%
6.0	16.41%
6.5	17.71%
7.0	18.70%
7.5	19.39%
8.0	19.70%
8.5	19.73%

Figure 36: Percentage variation of the air/water interface $\Delta A_\%$ as a function of the bumps' radius r_{bump} for different deposited droplet volumes.
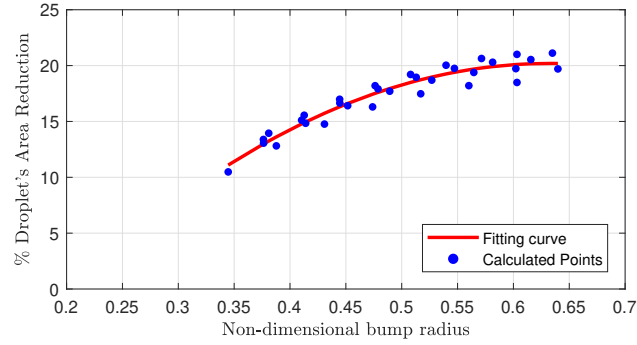

Figure 37: Percentage variation of the air/water interface $\Delta A_\%$ as a function of the non-dimensional bump radius r_{bump}^*.

CHAPTER 5

3D PRINTING

The numerical modeling of droplet spreading is further supplemented with experimental observations on a 3D-printed surface with same physical characteristics as the wet wall in the simulations.

5.1   Additive manufacturing application to surface micro-texturing

Since 1970s, nature has been one of the most inspiring sources for material engineers: many studies have mimicked natural surfaces' morphology for different functional purpose. The analysis of the lotus leaf is one such example that received a lot of attention and is related to wettability engineering, which is also goal of the current study.

Lantada et al. [18] combined Biomimetics and additive manufacturing techniques to obtain high precision biomimetic models, whose wettability is design-controllable. Their research concerned the lotus leaf's surface, whose hydrophobicity lead engineers to mimic its structure, in order to achieve materials with self-cleaning properties. This engineering marvel was recognized to such an extent that the physical phenomenon behind this kind of materials was itself called *Lotus Effect*.

3D direct laser writing is known to manage highly precise structures in a larger final size, producing at the same time a result with major reproduction accuracy. As a matter of fact, conventional surface refinement techniques, mainly consisting of either machining or coating,

do not concentrate on the surface morphology, reducing it to a consequence of the manufacturing process. By contrast, additive manufacturing can put into the foreground the surface micro-texture, especially in light of recent advances, which have also expanded the range of suitable materials for additive processes.

In conclusion, Lantada and his team's successful research inspired development of a 3D-printed model, mimicking the beetle's shell morphology. Subsequent analysis on such model is expected to provide insights on understanding droplet spreading and validate the numerical model shown in chapter 4.

5.2   NanoScribe Photonic Professional GT

For the last ten years, Additive Manufacturing (AM) technology has been among the most developing engineering fields, due to its revolutionary innovative approach to material manufacturing. All conventional production technologies, such as turning and milling, start from raw parts and transform them into the final product by removing material. Therefore, even the most precise process executed on the manufactured part to grind its surface determines the external refinement as a consequence of the process itself. By contrast, AM's approach, as its name suggests, is based on material addition, both handling the macroscopic features and enabling to concentrate on the surface's micro-texture. This last function can be accomplished because of the progress achieved in microscale AM.

The Nanotechnology Core Facility (NCF) at the University of Illinois at Chicago possesses a Photonic Professional GT 3D laser lithography system, produced by NanoScribe GmbH, a German company leading 3D printing on micro-, nano- and mesoscale machine manufacturing

sector. This 3D printer's working principle is based on two-photon polymerization (2PP) technology, enabling the production of high precision structures, with high submicrometer resolution and feature sizes down to $200\,nm$, the minimum spatial resolution available on the market [19]. Particularly, for 3D laser writing machines, which solidify polymeric material by means of a laser beam, the resolution is highly related to the voxel size, namely the dimension of the smallest unit of material that can be treated. Both these characteristics depend on the power consumed by the laser source, on the processed material properties and especially on the laser spot size. Such feature is achieved with lenses focusing the laser emission to the desired scale, by regulating its numerical aperture, called objectives. The Photonic Professional GT allows the user to choose among three objectives, identified by their magnifications: in ascending magnification (therefore precision) order, objectives 25x, 63x and 100x.

As stated above, the printer's objective moves the laser beam relative to the sample. Such function can be executed with two approaches, both implemented on the PPGT: when the printing substrate is moved with respect to the fixed focusing optics through a specifically engineered positioning unit, the printer is said to be working by *Fixed-Beam-Moving-Sample* (FBMS). On the contrary, if the laser beam itself is directed to the fixed sample, the approach is called *Moving-Beam-Fixed-Sample* (MBFS). The former approach certainly leads to higher-resolution structures, but requires longer printing time. Conversely, the latter accelerates the fabrication process, building the model *layer-by-layer*. The lateral movement of the laser beam is controlled by galvanometric mirrors, whereas piezo-actuators determine its vertical displacement.

Several resins are manufactured for the PPGT, although they result in different degrees of

precision [20]: ordinary photopolymers, also applied in the semiconductor industry and bio-compatible materials, give satisfying final outcome, but the best performance is achieved with the photoresists specifically developed by NanoScribe GmbH (such as IP-L, IP-L 780, IP-G, IP-G 780 and IP-Dip), in terms of both resolution and writing speed.

Similarly, the printing substrate, on which the machine solidifies the photopolymer, is chosen with reference to the manufactured part application: when the interest is to join the substrate itself with an optical or mechanical 3D-printed part, opaque IC-wafers are ideal. On the other hand, if the substrate must only support the printed part, a transparent glass is suitable, occasionally coated with specific composite, such as ITO.

To sum up, the exceptional performances of PPGT make it perfect for manufacturing micro-textures in the investigated beetle's shell scale, characterized by $10\,\mu m$ features.

5.3 Micro-textured model description

With reference to the features of the available equipment, a three-dimensional model of the beetle's shell was developed, through the CAD program *SolidWorks* (Dassault Systèmes). Despite its high performances, it is important to underline that the PPGT imposed several constraints. Essentially, two issues represented a limitation to the printing fulfillment:

- STL file size: the software used to read the input data and elaborate the printing information for the machine (*NanoScribe DeScribe*) cannot manage very large files, due to insufficient computational capacity;

- Printing time: because of the bumpy geometry's complexity, much time is required for the printing process. Hence, too large samples are not economically convenient, as the final cost is proportional to the time of use of the machine.

Thus, a compromise between printability and usability of the model was needed: as a result, a bumpy plate was designed, characterized by a $1,010 \times 997 \, \mu m^2$ area. As can be seen in Figure 38, its micro-texture was modelled recalling the characterizing bumps on the beetles' shell, as well as the wet wall designed for SE-FIT simulations. This way, the simulated and the live observed liquid/solid interaction are comparable.

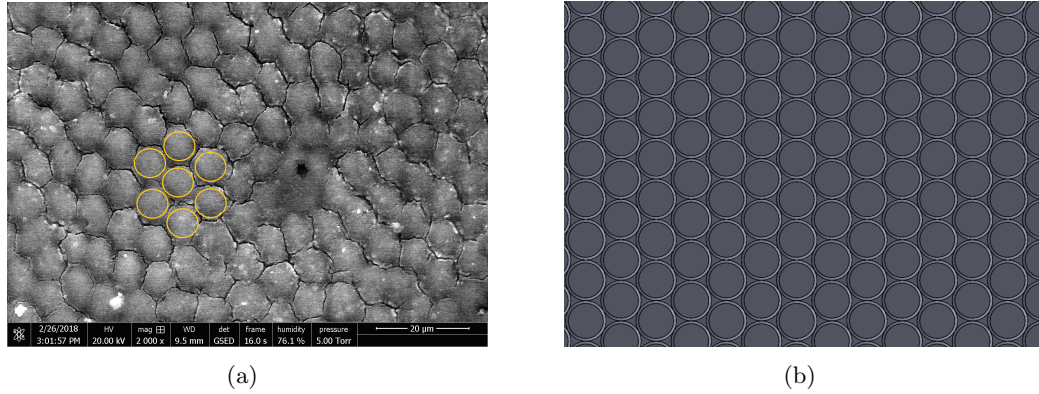| (a) | (b) |

Figure 38: Comparison between (a) the actual observed beetle's shell morphology, and (b) the designed and 3D-printed bumpy micro-texture.

Observing the elytron, one can individuate a hexagonal bump pattern, highlighted in Figure 38a. Therefore, the model was obtained by drawing a unit of six bumps equally spaced around a
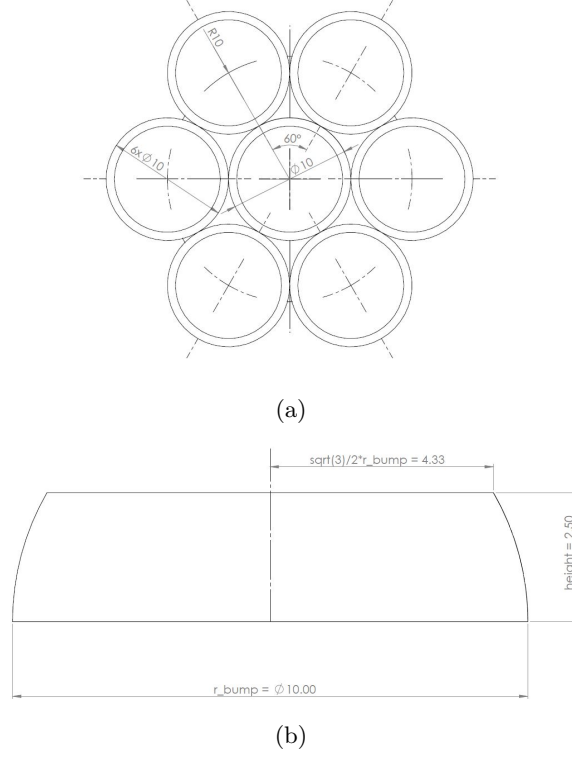
(a)

(b)

Figure 39: Elytron-shaped model's schematic (dimensions expressed in μm): (a) Top view: unit group of bumps, hexagonally distributed around the central one; (b) Side view: axial section of a bump with literal names for the primary variables (r_bump and $height$) corresponding to those used in SE-FIT simulations.

central one (Figure 39a). Then, such unitary set of bumps was repeated along the two horizontal directions, achieving the result shown in figure Figure 38b and Figure 40.

5.4   Printing procedure

Since SolidWorks' algorithm is not optimal for converting part files into STL ones, *Autodesk Fusion 360* was used to export the model. Then, it was fed into DeScribe, the software embed-

Figure 40: Isometric view of the micro-textured 3D CAD model, obtained through linear pattern of the *unit cell* shown in Figure 39a.

ded in the Photonic Professional GT. This program elaborates the designed model and allows to choose the printing parameters:

- **Objective**: the type of objective influences the printing accuracy. A lens not focusing enough the laser beam does not enable it to properly solidify the special tailored materials by NanoScribe. Each objective works with a different photopolymer: the desired model's dimensions required the most precise objective 63x, working with a photoresist named IP-Dip, which is the same used by Lantada, Hengsbach and Bade for their lotus leaf-shaped model. From their study, it was known that the wettability of IP-Dip is close to the one of the beetle's shell ($\theta_E = 70°$, equilibrium contact angle), having a 72° contact angle [18]. Therefore, IP-Dip was used as the material for our application.

- **Slicing distance**: the thickness of each polymer layer, set at 0.3 μm.

- **Hatching distance**: the space between adjacent tracks of material, set at 0.2 μm.
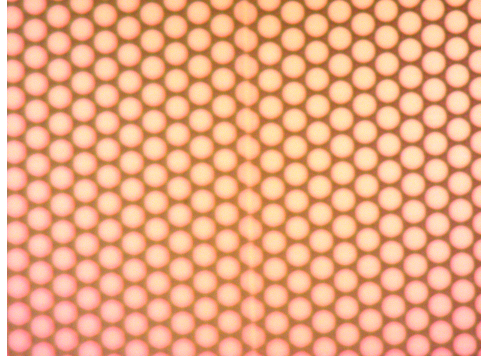
Figure 41: Detail of a stitching line on the printed model in the center of the image.

Subsequently, *DeScribe* generated a preview of the printed result, before dividing the whole model into $134 \times 134 \, \mu m^2$ writing fields: the objective indeed concentrates on one field at a time, stitching them together as precisely as possible. In fact, the stitching process is very critical in 3D-printing, especially at the microscale: bad stitched fields might result in imperfections compromising the texture's accuracy. An example of stitching line in the obtained model can be seen in Figure 41.

Lastly, after some elaborations, the software showed a graphic rendering of the final result, with an estimation of the printing time, $4h\,54min$ for the designed model, as shown in Figure 42.

DeScribe generated the required files in NanoScribe's proprietary format *General Writing Language* (*.gwl*), containing the structural design necessary to the machine. Finally, these files were fed into a second embedded software, called *NanoWrite*, which read the data and controlled the print job. The printing process took about 5 hours after which the sample was ready for experiments.
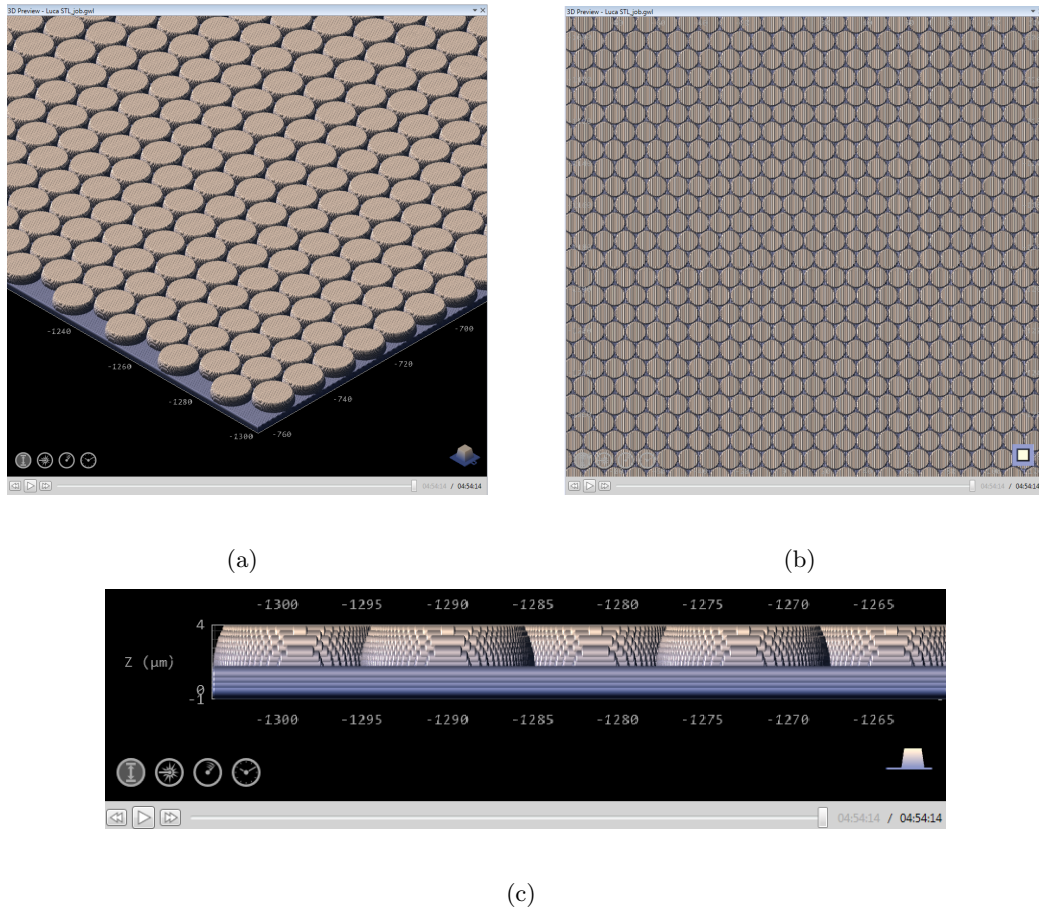
(a)

(b)

(c)

Figure 42: Bumpy surface 3D printing preview, illustrating the polymer sample: (a) Isometric view detail; (b) Top view for comparison with Figure 38; (c) Side view of the bumpy surface, showing the rendered bumps.
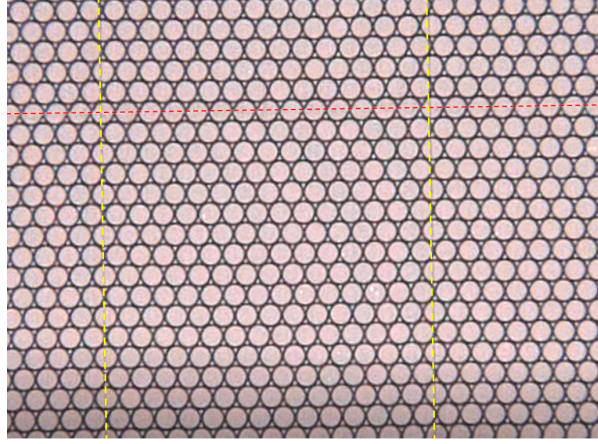
Figure 43: Microscope image of the 3D-printed micro-texture: two well-executed vertical stitching lines are indicated by yellow dashed lines and an imperfect horizontal one is highlighted in red.

5.5   Observation of water deposition on the printed surface

Water interaction was observed by inspecting the printed micro-textured surface with NCF's microscope *Keyence VHX-5000*. Fog was created using a household humidifier (manufactured by *PureGuardian*). The fog blast contains water droplets of diameter $20\,\mu m - 100\,\mu m$ range. After putting the supporting substrate on the microscope's horizontal stage, the objective was directed on the the printed model, with a 200x magnification, showing its morphology (Figure 43). Subsequently, the fog was guided onto the bumpy plate. It is important to underline that in this experiment the analyzed surface was maintained horizontal, tangentially hit by the mist flow, whereas the beetle actually positions itself in such a way that its shell is

perpendicular to the fog-harvesting wind. Water deposited on the bumpy surface, on the flat plate of IP-Dip and on the glass substrate, showing different characteristics on each of them, which could be captured in images and videos through the microscope.
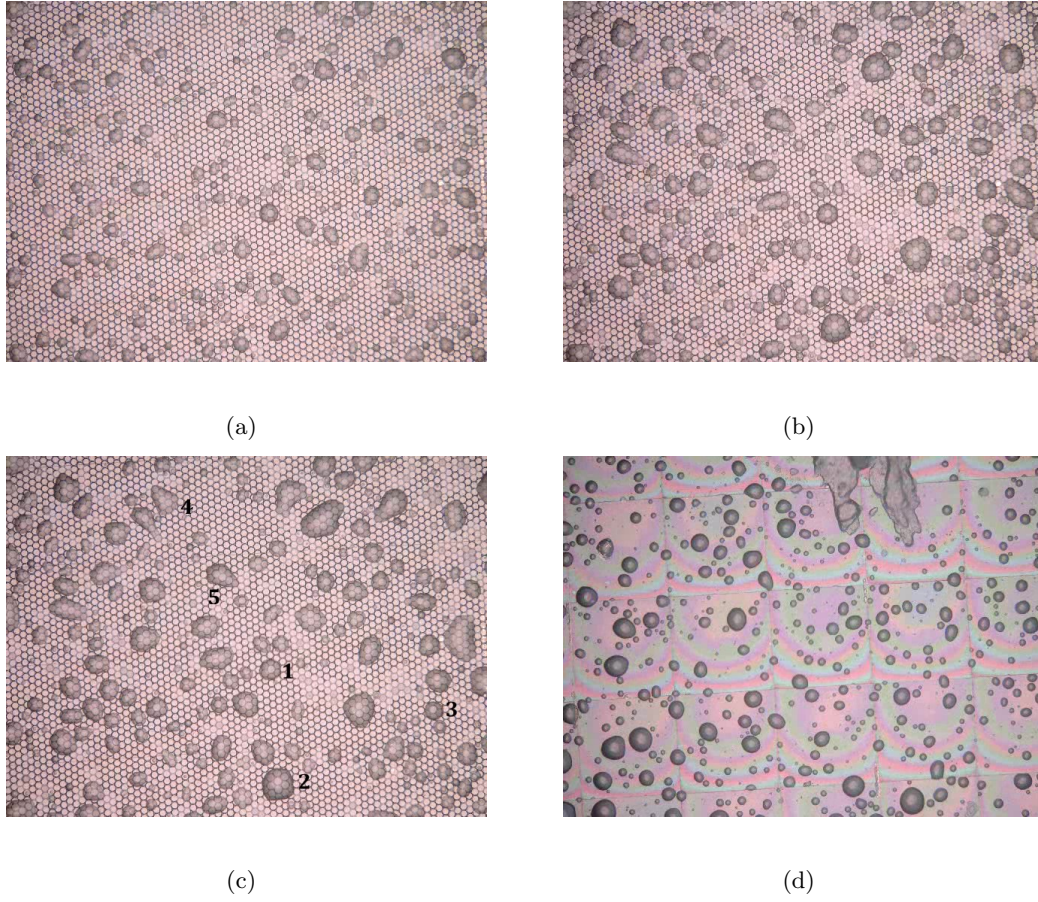

(a)

(b)

(c)

(d)

Figure 44: Sequence of water depositing on the 3D-printed bumpy model, been exposed to fog flow for (a) $20\,s$, (b) 30, (c) $35\,s$; (d) flat IP-Dip plate after $35\,s$ fog exposition (magnification 200x, each small circle in (a) has $10\,\mu m$ diameter).

As can be seen in Figure 44, it is firstly noticeable that the droplets seem to coalesce more on the bumpy model. Comparing Figure 44c and Figure 44d, one can observe that the two surfaces after $35\,s$ have both collected water, although the number of droplets on the smooth model is higher than on the bumpy one. However, dimension of each droplet is smaller on the flat plate, and the shape resembles closely to a spherical cap as compared to the bumpy one. At the same time, in Figure 44c the droplets' shape is more variable. Water tends to fill the grooves between the bumps, but when these are saturated, droplets start to form on the bumps themselves. Particularly, when the droplet is roughly centered on a bump (for instance droplets number 1, 2 and 3 in Figure 44c) its shape resembles the nearly axisymmetric configuration predicted by the SE-FIT simulations, as shown in 4. On the other hand, droplets look more irregular and asymmetric when their growth and coalescence occur in random direction (for example droplets number 4 and 5 in Figure 44c).

In conclusion, the micro-texture created by the bumps seems to increase water coalescence, which forms larger droplets on the irregular surface and the nearly axisymmetric droplet spreading showed similar configuration as predicted by SE-FIT. Experimental observation with parametric variation is time consuming and expensive. Hence, only one sample is compared with SE-FIT simulation and further experimental investigation is left as a future exercise.

CHAPTER 6

CONCLUSION

The present study analyzed the behavior of water droplets interacting with a micro-textured surface inspired by fog-harvesting desert beetle shell. In order to understand the phenomenon, numerical modeling of water contact was executed through open source software, writing computational simulations in Visual BASIC .NET programming language (GUI named SE-FIT). Additionally, 3D-printed micro-models were manufactured to further supplement the model results with experimental observations.

Results from the simulations suggest that the investigated micro-texture reduces the air/water interfacial area of an equilibrated droplet as compared to that on a smooth surface for the same volume of droplet. This outcome could have consequences on the evaporation of deposited water droplets, which is related to the number of water molecules exposed to air and able to escape from the liquid phase. Natural selection might have led beetles to adapt to Namib desert life, developing bumpy shells to reduce evaporation rate and retain more water on their body. Micrographs of water depositing on 3D-printed samples showed a remarkable increase in coalescence for the droplets collected by the biomimetic model, partially confirming the evaporation reduction.

It was also possible to assess how the distance between the bumps affects the droplet lateral area decrease: bringing the bumps closer together, a higher benefit is obtained for interface surface shrinkage. This would explain the morphology of the beetle shell, where the bumps

are packed together separated by tiny grooves. However, the most outstanding effect is caused by the bumps' radius, which can lead up to 20% reduction in area exposed to air if properly chosen. For this purpose, an engineering design criterion was developed, to optimize the effect of the micro-texture on droplet lateral area decrease.

Research continuously evolves: hence, further developments may be conducted, particularly in computational simulations. To begin with, the present thesis focuses exclusively on droplets centrally placed on a bump and spreading on the surrounding ones. Thus, it would be interesting to inspect the behavior of offset droplets formed on the bumpy surface, namely droplets centered off bumps' centers. This may lead to comprehend whether a relation between droplets' shape and lateral area reduction exists. Secondly, multiple droplet coalescence on the micro-textured model might be observed through computational analysis, to witness capillarity dynamic phenomena on a small scale. Finally, implementing different contact angles for the bump tips and valleys may lead to assess the presence of a wettability patterning on the beetle elytron, by comparing the equilibrium droplet shape and exposed area.

APPENDIX

PERMISSIONS TO USE COPYRIGHTED MATERIAL

APPENDIX (continued)

PERMISSION/LICENSE IS GRANTED FOR YOUR ORDER AT NO CHARGE

Copyright
Clearance
Center

RightsLink

Home | Account Info | Help

ACS Publications
Most Trusted. Most Cited. Most Read.

Title: Contact Angles on Spherical Surfaces

Author: C. W. Extrand, Sung In Moon

Publication: Langmuir

Publisher: American Chemical Society

Date: Sep 1, 2008

Copyright © 2008, American Chemical Society

Logged in as:
Luca Bellora
Account #:
3001277301

LOGOUT

PERMISSION/LICENSE IS GRANTED FOR YOUR ORDER AT NO CHARGE

This type of permission/license, instead of the standard Terms & Conditions, is sent to you because no fee is being charged for your order. Please note the following:

- Permission is granted for your request in both print and electronic formats, and translations.
- If figures and/or tables were requested, they may be adapted or used in part.
- Please print this page for your records and send a copy of it to your publisher/graduate school.
- Appropriate credit for the requested material should be given as follows: "Reprinted (adapted) with permission from (COMPLETE REFERENCE CITATION). Copyright (YEAR) American Chemical Society." Insert appropriate information in place of the capitalized words.
- One-time permission is granted only for the use specified in your request. No additional uses are granted (such as derivative works or other editions). For any other uses, please submit a new request.

If credit is given to another source for the material you requested, permission must be obtained from that source.

BACK | CLOSE WINDOW

CITED LITERATURE

1. Law, K.-Y.: Definitions for hydrophilicity, hydrophobicity, and superhydrophobicity: getting the basics right, 2014.

2. Extrand, C. and Moon, S. I.: Contact angles on spherical surfaces. Langmuir, 24(17):9470–9473, 2008.

3. Velcro: About Velcro brand, 2018. `https://www.velcro.com/about-us/our-brand/`, [Online; accessed 04/15/2018].

4. AskNature team: High speed train silently slices through air, 2016. `https://asknature.org/idea/shinkansen-train/#.WtocNIjwZPY`, [Online; accessed 04/15/2018].

5. 3M: 3M Wind Erosion Solutions, 2015. `http://multimedia.3m.com/mws/media/800189O/3m-wind-erosion-solutions.pdf`, [Online; accessed 04/15/2018].

6. Hamilton III, W. J. and Seely, M. K.: Fog basking by the namib desert beetle, onymacris unguicularis. Nature, 262(5566):284, 1976.

7. Parker, A. R. and Lawrence, C. R.: Water capture by a desert beetle. Nature, 414(6859):33, 2001.

8. Yanko Design: Dew Bank: Beetle Juice Inspired!, 2010. `http://www.yankodesign.com/2010/07/05/beetle-juice-inspired/`, [Online; accessed 02/25/2018].

9. de Gennes, P., Brochard-Wyart, F., and Quere, D.: Capillarity and Wetting Phenomena: Drops, Bubbles, Pearls, Waves. Springer New York, 2003.

10. Quéré, D.: Wetting and roughness. Annu. Rev. Mater. Res., 38:71–99, 2008.

11. Chen, Y., Schaeffer, B. M., Jenson, R., and Weislogel, M. M.: Surface Evolver - Fluid Interface Tool Version 1.112 User's Manual. Department of Mechanical and Materials Engineering, Portland State University, October 2012.

CITED LITERATURE (continued)

12. Canuto, C.: Notes of the Lecture Course Numerical Models and Methods (Mechanical Engineering. Dipartimento di Scienze Matematiche, Politecnico di Torino, March 2014.

13. Steinhauser, M.: Computational Multiscale Modeling of Fluids and Solids: Theory and Applications. Springer Berlin Heidelberg, 2016.

14. Brakke, K. A.: Surface Evolver Manual Version 2.70. Mathematics Department, Susquehanna University, August 2013.

15. Canuto, C. and Tabacco, A.: Analisi Matematica II: Teoria ed esercizi. Springer Milan, 2014.

16. Sun, M., Liang, A., Watson, G. S., Watson, J. A., Zheng, Y., and Jiang, L.: Compound microstructures and wax layer of beetle elytral surfaces and their influence on wetting properties. PloS one, 7(10):e46710, 2012.

17. Wolfram Research: Spherical Cap, 2018. `http://mathworld.wolfram.com/SphericalCap.html`, [Online; accessed 04/03/2018].

18. Lantada, A. D., Hengsbach, S., and Bade, K.: Lotus-on-chip: computer-aided design and 3d direct laser writing of bioinspired surfaces for controlling the wettability of materials and devices. Bioinspiration & Biomimetics, 12(6):066004, 2017.

19. NanoScribe GmbH: NanoScribe Photonic Professional GT: Technology, 2018. `https://www.nanoscribe.de/en/technology/additive-manufacturing/`, [Online; accessed 04/05/2018].

20. NanoScribe GmbH: NanoScribe Photonic Professional GT: Materials & Processes, 2018. `https://www.nanoscribe.de/en/technology/materials/`, [Online; accessed 04/05/2018].

VITA

NAME	Luca Bellora
EDUCATION	
	Master of Science in Mechanical Engineering, University of Illinois at Chicago (UIC), Chicago, IL, USA, August 2018
	Master of Science in Mechanical Engineering, Politecnico di Torino (POLITO), Turin, Italy, July 2018
	Bachelor of Science in Mechanical Engineering, Politecnico di Torino, Turin, Italy, October 2016
LANGUAGE SKILLS	
Italian	Native speaker
English	Full working proficiency
	2016 - IELTS examination (7.5/9)
	A.Y. 2017/18 Achieved Master's degree at the UIC, Chicago, Illinois, USA
	A.Y. 2016/17 Attended classes exclusively in English at POLITO, Turin, Italy.
SCHOLARSHIPS	
Spring 2017	Italian scholarship for TOP-UIC students
TECHNICAL SKILLS	
Intermediate level	C, Python
Advanced level	MATLAB, AutoCAD, LaTeX
Proficient level	SolidWorks, MS Office (Microsoft Word, Excel, PowerPoint, Outlook)
CERTIFICATIONS	
June 2016	Certified SolidWorks Associate for Mechanical Design

VITA (continued)

ACADEMIC PROJECTS

Fall 2017	Stochastic Analysis of a Truss to Determine its Reliability: managed statistically known Young modules and loads through Monte Carlo interations of the FEM to determine the Probability Distribution Functions of the nodes' horizontal and vertical deflection; utilized MATLAB for computations and graphs; determined the maximum allowed deflections to have an acceptable probability of failure, defined by the practice circumstances.
Spring 2017	Assessment of a Hydropower Plant's Kaplan Turbine's Speed Increaser: inspected static and fatigue strength of the shafts, planetary gear train, and bearings, according to the reference FKM regulation; executed corrections in the gear modular proportioning, due to observed insufficient performance; drew the transmission system on SolidWorks, managing Geometric Dimensioning and Tolerancing (GD&T) through SolidWorks Model Based Definition (MBD).
Spring 2017	Solar Energy Equipment: conceived collector-based hot tap water heating system for an apartment building; accomplished Energetic analysis for heating requirements and optimized the plant through Exergetic Analysis; modelled heat transfer phenomena through FEM-based simulations on MATLAB.
Summer 2016	BS Thesis, Mechanical Characterization of Carbon Nanotube Polyurethane Foams: tested the aerospace transmission application feasibility for composite materials developed by the University of Bristol, Bristol, UK; executed compression tests to determine Young Modulus and Stiffness on MTS QTest/10 machine, produced by MTS Systems Corporation; observed that the carbon nanotubes reinforcement improves polyurethanes damping properties.
Spring 2016	Development of a Drone Manufacturing Factory: designed product-customized production plant and relative heating and electrical systems; engineered plant layout on AutoCAD according to manufacturing process; accomplished Production Time analysis with Microsoft Excel spreadsheets; computed air conditioning requirement and chose heating machines from manufacturers catalogue.